TNF-α-induced type I IFN signalling decreases neurogenesis and drives T cell chemotaxis

Tinne Amalie Damgaard Nissen[1,2], Arishma Baig[1], Daniel T. Rock[2], Sandra Shibu[2], Hyunah Lee[2], Lauren A. O'Neill[1], Susan John[3], Linda S. Klavinskis[1]*, Sandrine Thuret[2]*

[1] Department of Infectious Diseases, School of Immunology & Microbial Sciences, King's College London, London SE1 9RT, UK

[2] Department of Basic and Clinical Neuroscience, Institute of Psychiatry, Psychology and Neuroscience, King's College London, London SE5 9RT, UK

[3] Peter Gorer Department of Immunobiology, King's College London, London SE1 9RT, UK

*Equally contributed and co-corresponding authors. Linda.Klavinskis@kcl.ac.uk and Sandrine.1.thuret@kcl.ac.uk

Abstract

Adult hippocampal neurogenesis (AHN) is essential for learning, memory, and mood regulation, and its disruption is implicated in ageing, neurodegeneration, and mood disorders. However, the mechanisms linking inflammation to AHN impairment remain unclear. Here, we identify chronic tumour necrosis factor-alpha (TNF-α) signalling as a key driver of neurogenic dysregulation via a previously unrecognized type I interferon (IFN) autocrine/paracrine loop in human hippocampal progenitor cells (HPCs). Using a human *in vitro* neurogenesis model, single-cell RNA sequencing, and functional T cell migration assays, we show that TNF-α induces a robust type I IFN response in HPCs, promoting chemokine and CXCR3-dependent T cell recruitment and suppressing

neurogenesis. This inflammatory signalling cascade drives a fate switch in HPCs from a neurogenic trajectory towards an immune-defensive phenotype, with critical implications for infectious and inflammatory disease pathogenesis. These findings uncover a key inflammatory checkpoint regulating human AHN and highlight potential therapeutic targets to restore neurogenesis in chronic inflammatory states.

Introduction

Adult neurogenesis occurs in two main neurogenic niches in the mammalian brain: the subventricular zone (SVZ) lining the lateral ventricles and the subgranular zone (SGZ) of the dentate gyrus of the hippocampus[1]. Upon activation, hippocampal neural stem cells (NSCs) known as radial glia-like cells (RGLs) divide and differentiate into astrocytes or excitatory, glutamatergic neurons integrating into the granule cell layer (GCL). While adult hippocampal neurogenesis (AHN) was first discovered in rodents[2], studies have since demonstrated human AHN using birth dating with C^{14} [3], immunofluorescence of postmortem tissue[4–7], *in vitro* propagation of NPCs from adult human postmortem tissue[8], and single nucleus RNA sequencing[9]. However, other studies have failed to detect human AHN[10,11]. This discrepancy could be due to postmortem delay, fixation protocols, or lifestyle/health status of subjects from which the brain tissue was obtained[12]. AHN in rodents enhances various cognitive functions including memory and learning[13], object recognition[14], and mood regulation[15]. Less is known about the functional role of AHN in humans. One study found that the number of neuroblasts was reduced in humans with cognitive impairments, whereas higher numbers of neuroblasts were associated with better cognitive status[7].

AHN perturbations have been observed in brain ageing, neurodegenerative disorders, and mood disorders[16,17]. Given the role of AHN in memory and mood regulation, the AHN perturbations observed in ageing, neurodegenerative disorders, and mood disorders have been suggested to contribute to age-associated cognitive decline and patient symptoms. This idea is supported by studies demonstrating that increasing AHN is sufficient to reduce depressive-like behaviours[18] and that boosting AHN as well as activating adult-born neurons ameliorates Alzheimer's disease (AD) symptoms in mice[19]. Inflammation is elevated in AD[20], ageing[21], and in some patients suffering from mood disorders such as depression[22]. In particular, the proinflammatory cytokine TNF-α has been implicated in AD[23,24] and depression[25,26]. Inflammatory cytokines such as TNF-α, have been found to negatively regulate AHN[27,28]. Therefore, inflammation-induced AHN perturbations have been proposed as a converging mechanism driving patient symptoms. Targeting inflammation-induced AHN perturbations in ageing, neurodegenerative disease, and mood disorders presents a novel, interesting target for the development of neuroprotective therapy[16]. Therefore, understanding the molecular mechanisms by which key inflammatory mediators such as TNF-α change the cell fate of hippocampal NSCs is a prerequisite for developing novel therapies aimed at preserving AHN and associated cognitive functions in an inflammatory milieu.

Chronic TNF-α-mediated inflammation was recently shown to drive a functional switch in olfactory NSCs from neuroregeneration to immune function *in vivo*[29]. The olfactory NSCs were found to play a direct role in recruiting inflammatory cells, including T cells, at the expense of switching off their neuroregenerative function. We hypothesised that chronic TNF-α-mediated inflammation could drive a similar functional switch in human HPCs,

from neurogenesis to immune function. Such a cell fate switch could explain the altered AHN observed in ageing, AD, and depression where TNF-α levels are chronically elevated and offer a novel explanation for the infiltration of T cells in neurogenic niches in ageing and neurodegenerative disease[30–32].

Here, we used an *in vitro* model of human hippocampal neurogenesis to investigate the hypothesis that chronic TNF-α can drive a switch from neurogenesis towards immune function and to uncover molecular mechanisms involved. We found that chronic TNF-α decreased neurogenesis and stimulated the secretion of high levels of CXCL10. Using scRNA sequencing, we identified TNF-α-induced type I IFN signalling in HPCs. We demonstrate that TNF-α drives type I IFN signalling in HPCs via an autocrine/paracrine loop not previously described in CNS resident cells. The TNF-α-induced autocrine/paracrine type I IFN signalling loop mediated the secretion of chemokines driving CXCR3-dependent chemotaxis of primary human T cells and the antineurogenic effects of chronic TNF-α. Collectively, our data support the hypothesis that chronic TNF-α can drive a functional switch in human HPCs away from neurogenesis towards immune function and demonstrate that TNF-α-induced type I IFN signalling is a key molecular mechanism underlying the switch.

Results

Functional and phenotypic reprogramming of HPCs driven by TNF-α

To investigate how TNF-α reprograms human HPCs, we first confirmed that our cellular model expressed the TNF-α receptors TNFR1 and TNFR2 (Supplementary Fig. 1). The cells were TNF-α-responsive as 30 minutes of treatment led to a peak in the fraction of

nuclear NF-κB p65 fluorescence (Fig. 1A-B). The fraction of nuclear NF-κB p65 fluorescence remained elevated after 24 hours and 48 hours of treatment as previously observed for foetal brain-derived primary human NPCs[33]. This prolonged canonical NF-κB pathway activation could be mediated by autocrine loops activated downstream of TNF-α. To address the functional relevance of TNF-α-induced signalling in the HPCs and their differentiated progeny, we evaluated the secretion of the NF-κB regulated cytokine IL-6 and a panel of NF-κB regulated chemokines. The levels of IL-6 and chemokines were analysed in the supernatant 24 hours and 48 hours after TNF-α treatment of the HPCs, as well as 24 hours, 48 hours, and seven days of TNF-α treatment in differentiating HPCs (Supplementary Fig. 2). We found that HPCs and their differentiated progeny secreted IL-6 and several chemokines in response to TNF-α (Supplementary Fig. 3-5). Among the panel of chemokines analysed, CXCL10 was secreted at the highest levels in response to TNF-α (Fig. 1C – D). Next, we investigated how chronic exposure to TNF-α affected the neuronal differentiation of HPCs. The HPCs were cultured under proliferation conditions for 48 hours ± TNF-α, before inducing their differentiation for seven days where cells were treated ± TNF-α every 48 hours (Fig. 1E). We found that chronic exposure to TNF-α dose-dependently decreased the percentage of differentiated cells expressing the neuroblast-specific marker doublecortin (DCX) (Fig. 1G). In contrast, only chronic exposure to 10 ng/ml TNF-α led to a decrease in the percentage of differentiated cells expressing the neuronal marker microtubule-associated protein 2 (MAP2) (Fig. 1H). In addition to a decrease in the percentage of cells expressing neuronal markers, we found that chronic TNF-α significantly reduced the total neurite length of both DCX+ and MAP2+ cells indicative of impaired morphological maturation (Supplementary Fig. 6). Collectively,

these data demonstrated functional and phenotypic reprogramming of HPCs in response to TNF-α.

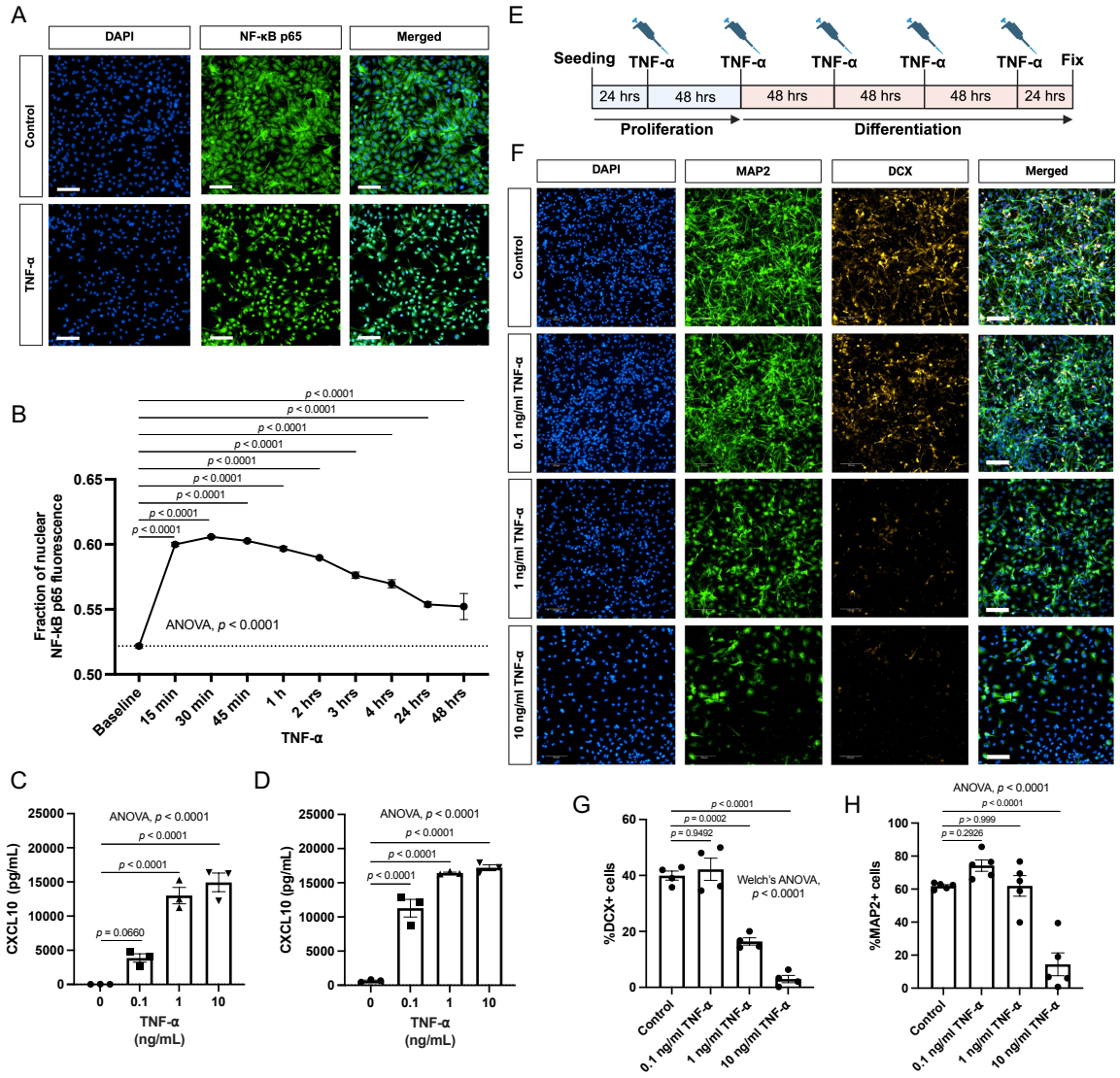

Fig. 1 | TNF-α drives immune signalling and decreases neurogenesis in human hippocampal progenitor cells. A Representative immunocytochemistry images of three independent experiments with similar results showing the expression of NF-κB p65 on HPCs treated ± 10 ng/ml TNF-α for 15 minutes. Scale bar represents 100 µm. **B** Quantification of the fraction of nuclear NF-κB p65 fluorescence intensity relative to total cellular fluorescence. Data represent mean ± SEM from *n* = 3. Statistical analysis: one-way ANOVA followed by Bonferroni multiple comparisons test. **C** and **D** Quantification of CXCL10 levels in culture supernatants measured by ELISA. **C** HPCs under proliferation conditions treated for 48 hours ± 0.1, 1, or 10 ng/ml TNF-α. **D** HPCs under differentiation conditions treated for 7 days ± 0.1, 1, or 10 ng/ml TNF-α. Data represent mean ± SEM from *n* = 3. Statistical analysis: one-way ANOVA followed by Bonferroni multiple comparisons test. **E** Schematic overview of the chronic TNF-α treatment regime for investigating its effect on neuronal differentiation. HPCs were treated under proliferation conditions for 48 hours ± 0.1, 1, or 10 ng/ml TNF-α before inducing differentiation for seven days under treatment ± 0.1, 1, or 10 ng/ml TNF-α every 48 hours. **F** Representative images showing the expression of MAP2 (green) and DCX (orange) on seven days differentiated HPCs treated chronically ± 0.1, 1, or 10 ng/ml TNF-α. Scale bar represents 100 µm. **G** and **H** Quantification of the percentage of DCX+ cells and MAP2+ cells respectively based on **F**. Data represent mean ± SEM from. **G** Data based on *n* = 4. Statistical analysis: Welch's ANOVA followed by Games-Howell post-hoc test for pairwise comparisons. **H** Data based on *n* = 5. Statistical analysis: one-way ANOVA followed by Bonferroni multiple comparisons test.

Single-cell RNA sequencing uncovered impaired neuronal differentiation and upregulation of IFN-regulated genes in response to chronic TNF-α

To uncover molecular mechanisms underpinning the effects of chronic TNF-α on HPCs and their differentiated progeny we performed an exploratory scRNA sequencing experiment. We investigated how exposure to chronic 0.1 ng/ml (referred to as low TNF) and 1 ng/ml TNF-α (referred to as high TNF) affected HPCs (48 hours of treatment) as well as their differentiated progeny after 7 and 14 days of differentiation (TNF-α treatment every 48 hours) (Fig. 2A). After quality control, a total of 26,376 genes across 22,133 cells were left. We identified 15 cell clusters (Fig. 2B) and observed the expected cell types including radial glial-like cells (RGLs), intermediate progenitor cells (IPCs), neuroblasts, immature neurons, and astrocytes. Cluster 1, 2, 3, and 4 were astrocyte-like clusters based on their expression of astrocytic genes including *GFAP*, *AQP4*, and *S100B* (Fig. 2D). Cluster 5 and 6 were RGL/NSC-like cells based on the expression of *FABP7*, *PTN*, *CDH4*, and *HES1* (Fig. 2D). Cluster 7, 8, 9, and 10 were IPC-like clusters based on their expression of *HMGB2*, *MKI67*, and *STMN1*. Cluster 11 was neuroblast-like based on its expression of *DCX* and *PROX1*, whereas cluster 12 was immature neuronal-like based on its expression of *CALB2*, *NRXN3*, and *MAP2*. Cluster 13, 14 and 15 which originated from the samples of cells differentiated in the presence of chronic 1 ng/ml TNF-α did not align transcriptionally with the signature of the astrocytic, neuroblast, or immature neuron clusters (Fig. 2D), which could suggest that chronic TNF-α signalling disrupted normal lineage commitment and differentiation leading to transcriptionally dysregulated states. Cluster 13 and cluster 14 expressed *ID4*, *CLU*, and *PTN* indicative of an NSC/astrocyte-like identity, cluster 14 expressed *ID4*, *FABP7*, and *GFAP* similarly indicative of an

NSC/astrocyte-like identity, whereas cluster 15 did not express genes indicative of any of the identified cell types. Only a very limited number of cells originating from the samples differentiated in the presence of chronic 1 ng/ml TNF-α belonged to the neuroblast-like cluster 11 and the immature neuron-like cluster 12 (Fig. 2C). This finding indicated that chronic 1 ng/ml TNF-α impaired the normal neurogenic trajectories of the differentiating HPCs in line with the observed decrease in the percentage of DCX+ neuroblasts (Fig. 1G).

The control and low dose TNF-α (0.1 ng/ml) treated cells generally clustered together, whereas the cells treated with the higher dose TNF-α (1 ng/ml) clustered separately (Extended data Fig. 1A). Of the two RGL-like clusters, cluster 5 was constituted mainly of cells originating from the control and low dose TNF-α (0.1 ng/ml) treated HPCs and cluster 6 was constituted mainly of cells originating from the higher dose TNF-α (1 ng/ml) treated HPCs. Surprisingly, the top upregulated genes in cluster 6 as compared to cluster 5 included the classic type I interferon-stimulated genes *ISG15*, *ISG27*, *IFI6*, and *IFITM3* (Fig. 3A). In line with this finding, the biological process GO terms based on the upregulated genes included cellular response to type I interferon, defence response to virus, and regulation of viral process indicative of a classic type I interferon antiviral response signature (Extended data Fig. 1 F). The cellular compartment GO terms included MHC protein complex, proteasome complex, and phagocytic vesicle pointing to MHC class I antigen processing and presentation as well as phagocytosis which has recently been described for reactive, hippocampal NSCs[34].

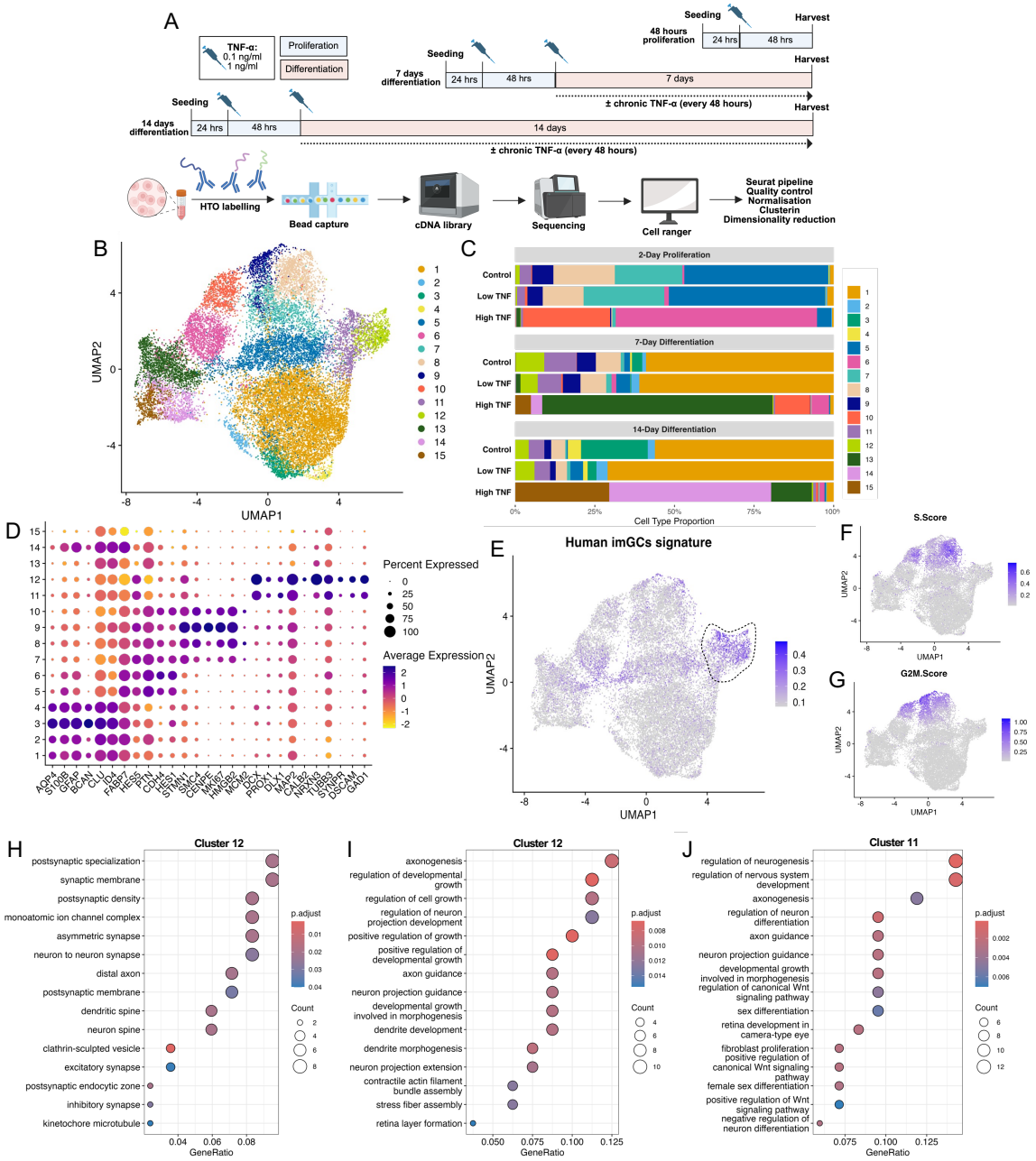

Fig. 2 | Chronic TNF-α impairs neuronal differentiation. A Schematic overview of the experimental design. **B** UMAP plot showing transcriptional clustering of single cells. Colors indicate the 15 cell clusters identified. **C** Stacked bar graphs showing the frequencies of cell clusters shown in **B** across the time and treatment groups. **D** Dot plot showing the expression of canonical marker genes for expected cell types across the cell clusters. **E** UMAP plot showing each cell scored against a human immature granule cells (imGCs) signature (Zhou et al 2022). The outlined area highlight the of the signature with cluster 11 and 12. Colour scale is truncated below the 50th percentile of expression (min.cutoff = "q50") to enhance visibility of high-expressing cells. **F** and **G** shows UMAP plots showing each cell scored against S phase genes and G2/M phase. Colour scale is truncated below the 10th percentile of expression (min.cutoff = "q10") to enhance visibility of high-expressing cells. **H** Dot plot showing gene ontology (GO) enrichment analysis of cellular component terms based on the top 100 genes positively defining cluster 12. **I** and **J** Dot plots showing GO enrichment analysis of biological process terms based on the top 100 genes positively defining cluster 12 and cluster 11 respectively.

Conversely, looking at the biological process GO terms for the top upregulated genes in cluster 5 as compared to cluster 6, several terms related to translation and ribosome biogenesis (Extended data Fig.1C). These are key processes involved in NSC activation[35,36]. This finding could indicate that the higher dose of TNF-α blocks NSC activation and promotes quiescence in line with recent findings[37]. Examining the upregulated genes of the IPC-like cluster 10 originating mainly from the higher dose TNF-α treated cells to the IPC-like cluster 7, 8, and 9 originating from the control and lower dose TNF-α treated HPCs showed similar results (Fig. 3B, Extended data Fig. G and I).

To better understand the functional identity of cluster 13, 14 and 15 which originated from the samples of cells differentiated in the presence of chronic 1 ng/ml TNF-α we investigated the biological GO terms for the clusters based on their cluster-specific genes. The GO terms for cluster 13 which was mainly constituted by cells originating from the 7-day differentiated cells included antiviral and type I IFN response as well as antigen processing and MHC class presentation indicating that the cells are pushed towards an aberrant, highly immune-reactive, and IFN-responsive transcriptional state (Fig. 3C). Similarly, GO enrichment analysis of cluster 14 originating mainly from the 14-day differentiated cells revealed a strong immune-related signature including the terms leukocyte mediated immunity and lymphocyte-mediated immunity (Fig. 3D). Finally, top GO terms for cluster 15 originating mainly from the 14-day differentiated cells included wound healing, collagen fibril organisation, and response to TNF-α (Fig. 3E). These terms could reflect a repair or injury-associated transcriptional state which has recently been observed in reactive astrocytes[38].

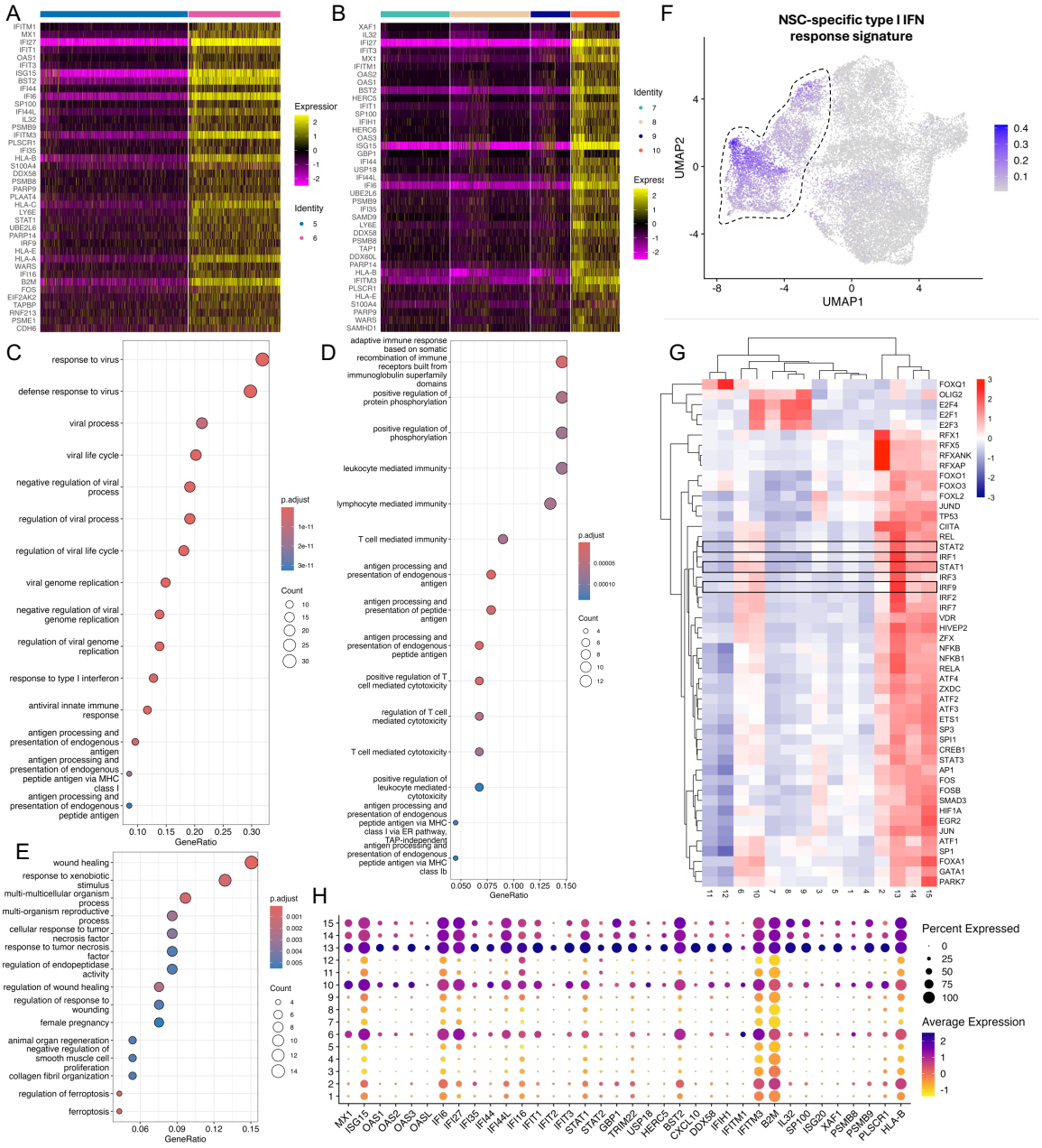

Fig. 3 | Chronic TNF-α drives the upregulation of type I IFN genes. A Heatmap of top 40 upregulated genes based on log fold change in cluster six as compared to cluster five. **B** Heatmap of top 40 upregulated genes based on log fold change in cluster ten as compared to cluster seven, eight, and nine. **C** Dot plot showing gene ontology (GO) enrichment analysis of biological processes terms based on the top 100 genes positively defining cluster 13. **D** Dot plot showing gene ontology (GO) enrichment analysis of biological processes terms based on the top 100 genes positively defining cluster 14. **E** Dot plot showing gene ontology (GO) enrichment analysis of biological processes terms based on the top 100 genes positively defining cluster 15. **F** UMAP plot showing each cell scored against a NSC IFN-β transcriptional signature. The outlined area highlight the of the signature with cluster 6, 10, 13, 14, and 15. Colour scale is truncated below the 10th percentile of expression (min.cutoff = "q10") to enhance visibility of high-expressing cells. **G** Heatmap showing the mean activity per cluster of the top 50 more variable transcription factors. STAT1, STAT2 and IRF9 is highlighted. **H** Dot plot showing the expression of interferon response genes across the cell clusters.

As TNF-α is not described to directly drive the expression of type I IFN genes, we hypothesised that type I IFN transcriptional signature could be driven by type I IFNs

upregulated downstream of TNF-α driving autocrine/paracrine signalling. The HPCs and differentiated progeny did express genes constituting the molecular machinery to respond to type I IFNs (Supplementary data Fig. 7). To this end, we scored the cells against a recently developed NSCs-specific type-I IFN response signature[39]. We found that the signature largely overlapped with the cell clusters originating from the samples of HPCs and differentiated progeny treated with the higher dose TNF-α (Fig. 3F). In line with the type-I IFN response signature, a transcription factor activity inference analysis predicted STAT1, STAT2, and IRF9 activity in the cell clusters specific to treatment with the higher dose of TNF-α (Fig. 3G). Similarly, we found a broad panel of interferon-stimulated genes (ISGs) upregulated in all cell clusters specific to treatment with the higher dose TNF-α (Fig. 3H). Collectively, these data indicated that TNF-α drove the upregulated of type I IFN response genes in HPCs and their differentiated progeny. Furthermore, chronic exposure to TNF-α impaired neurogenesis and drove differentiating HPCs towards an aberrant, highly immune-reactive transcriptional state deviating from that of the gliogenic and neurogenic clusters.

TNF-α drives type I IFN signalling through autocrine and paracrine activation of IFNAR

As STAT1 has been shown to negatively regulate human hippocampal neurogenesis[40] and STAT1/STAT2 activation drives the upregulation of type I IFN-regulated genes, we validated the predicted STAT1/STAT2 activation in HPCs in response to TNF-α. We found a delayed activation of STAT1/STAT2 after three to six hours of treatment (Fig. 4A - B and Extended data Fig. 2A - B) which supported an indirect mechanism of activation. In

line with our hypothesis of autocrine/paracrine signalling, we found that factors secreted in response to TNF-α increased the percentage of ISG15+ cells (Extended Data Fig. 2C – D). TNF-α transiently increased the expression of *IFNB1* peaking after three hours of treatment (Fig. 4B) supporting early findings[41–43]. The temporal correlation between the STAT1/STAT2 action and the *IFNB1* induction suggested secreted IFN-β as the likely mediator of the TNF-α-induced STAT1/STAT2 activation. We investigated the mechanism of the TNF-α-induced *IFNB1* induction and found it to be dependent on NF-κB signalling (Extended data Fig. 2E) and independent of *de novo* protein synthesis (Extended data Fig. 2F) in line with findings from murine bone-derived macrophages (BMDMs)[43]. TNF-α has previously been demonstrated to increase interferon-regulatory factor 1 (IRF1) expression[41,44,45], and IRF1 has been found to be indispensable for TNF-α-induced *IFNB1* induction[42,43]. We found that TNF-α upregulated the expression of *IRF1* in the HPCs after 1.5 hours peaking after 3 hours (Supplementary Fig. 11). Based on the temporality of the TNF-α-induced upregulation of *IRF1*, IRF1 could be important for the *IFNB1* induction in the HPCs. We hypothesised that secreted IFN-β could drive autocrine/paracrine type I IFN signalling and thereby upregulation of ISGs such as CXCL10 as demonstrated for fibroblast-like synoviocytes[45]. Analysing the temporal kinetics of the TNF-α-induced upregulation of *CXCL10* demonstrated the strongest upregulation after six hours of treatment (Fig. 4D). This delayed upregulation agreed with an indirect upregulation of *CXCL10* mediated by secreted IFN-β. After six hours of treatment with TNF-α, we found the *CXCL10* upregulation to be dependent on *de novo* protein synthesis (Fig. 4E), which further supported the autocrine/paracrine signalling driving the upregulation.

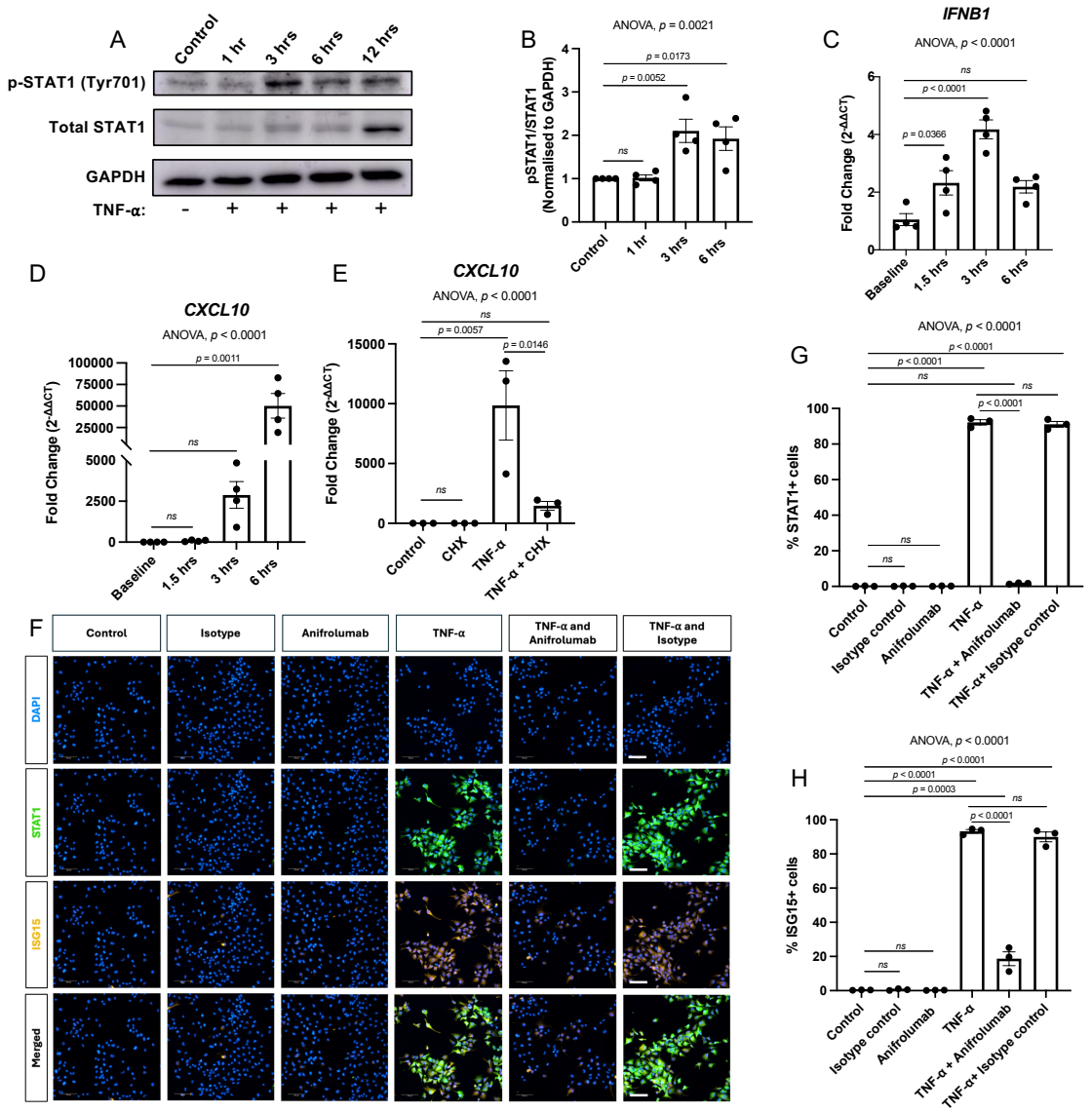

Fig. 4 | TNF-α drives type I IFN signaling in human hippocampal progenitor cells via autocrine/paracrine signalling via IFNAR. **A** Representative western blots of four independent experiments showing the activation of STAT1 in HPCs treated with 1 ng/ml TNF-α for 1 hr, 3 hrs, 6 hrs, and 12 hrs. Cell lysates were probed for phosphorylated STAT1 (p-STAT1 Tyr701), total STAT1, and GAPDH as a loading control. **B** Quantification of STAT1 activation in human hippocampal progenitor cells from **A**. pSTAT1 and STAT1 intensities were normalized to GAPDH intensity before calculating the fold change pSTAT1/STAT1 relative to control. Data represent mean ± SEM from four independent experiments. Statistical analysis: one-way ANOVA followed by Bonferroni's multiple comparisons. **C** RT-qPCR data showing the relative gene expression of *IFNB1* in response to treatment with 1 ng/ml TNF-α. Data is represented as mean ± SEM of four independent experiments. Statistical analysis: one-way ANOVA followed by Bonferroni's multiple comparisons. **D** RT-qPCR data showing the relative gene expression of *CXCL10* in response to treatment with 1 ng/ml TNF-α. Data is represented as mean ± SEM of four independent experiments. Statistical analysis: Kruskal-Wallis test followed by Dunn's post hoc correction. **E** RT-qPCR data showing the relative gene expression of *CXCL10* in HPCs treated for six hours with 10 µg/ml CHX or DMSO ± 1 ng/ml TNF-α. Data is represented as mean ± SEM of three independent experiments. Statistical analysis: one-way ANOVA followed by Bonferroni's multiple comparisons. **F** Representative images of three independent experiments with similar results showing the expression of STAT1 (green) and ISG15 (orange) on HPCs. Scale bar represents 100 µm. **G** Quantification of the percentage of STAT1+ cells based on **F**. Data represent mean ± SEM. Statistical analysis: one-way ANOVA followed by Bonferroni's multiple comparisons. **H** Quantification of the percentage of ISG15+ cells based on **F**. Data represent mean ± SEM. Statistical analysis: one-way ANOVA followed by Bonferroni's multiple comparisons.

To confirm the hypothesis of an autocrine/paracrine loop driving the type I IFN signalling, we treated HPCs for 24 hours with TNF-α in the absence or presence of the IFN-α/β

receptor (IFNAR) blocking antibody anifrolumab[46]. We found that IFNAR antagonism entirely blocked the TNF-α-induced upregulation of STAT1+ cells and largely attenuated the TNF-α-upregulation of ISG15+ cells (Fig. 4 F-H). Similarly, we found that blocking Janus protein tyrosine kinases (JAKs) downstream of IFNAR using JAK Inhibitor I[47] blocked the TNF-α-upregulation of ISG15+ cells (Extended Data Fig. 2 G - H). Finally, we found that TNF-α upregulated the type I IFN-induced tetherin/BST-2[48] on the cell surface of HPCs (Extended data Fig. 2I). Tetherin/BST-2 was recently identified as upregulated on the cell surface of dysfunctional NSCs in ageing neurogenic niches[30]. Collectively, these data demonstrated that TNF-α upregulated IFN-β in HPCs which signalled autocrine/paracrine via IFNAR and downstream JAKs to drive the expression of ISGs such as *CXCL10*.

TNF-α-conditioned media from HPCs and their differentiated progeny drive CXCR3-dependent chemotaxis of primary human T cells

After elucidating the molecular mechanism by which TNF-α drives type I IFN signalling in HPCs, we next investigated its functional consequences. Recent studies have highlighted that T cells infiltrate neurogenic niches in ageing and AD where they have been found near NSCs[30,32,49–53]. We found high levels of the type I IFN-regulated CXCL10 and CXCL11 in the supernatant of HPCs and their differentiated progeny in response to TNF-α. CXCL10 and CXCL11 can drive the chemotaxis of T cells by binding to the receptor CXCR3[54]. Therefore, we hypothesised that CXCL10 and CXCL11 secreted from HPCs and their differentiated progeny in response to TNF-α could drive CXCR3-dependent chemotaxis of activated T cells. We set up an *in vitro* transwell assay using primary human

T cells from three healthy donors (Supplementary Data Fig. 14). Naïve T cells do not express CXCR3, but the receptor is rapidly induced following activation and remains highly expressed on CD4+ helper T cells and CD8+ cytotoxic T cells[55]. Furthermore, CXCR3 is expressed on nearly all CD8+ T cells in the aged brain parenchyma[56].To validate our assay, we treated the cells with 1 μM CXCR3 antagonist AMG487[57] or DMSO control before placing the cells in the upper chamber of the transwell system (Fig. 5A). We then evaluated the chemotaxis of the T cells through a porous membrane towards 100 ng/ml recombinant human CXCL10 in the lower chamber. For the control-treated cells, the chemotactic index of CD4+ T cells and CD8+ T cells was significantly increased in response to the recombinant CXCL10 (Fig. 5B – C). However, we did not find an increase in the chemotactic index for CD4+ T cells and CD8+ T cells pre-treated with the CXCR3 antagonist. These data demonstrated that the assay delivered consistent results across the three donors.

Next, we generated conditioned media (CM) from control-treated and TNF-α-treated HPCs (Fig. 5D). We asked if chemokines in the TNF-α-CM were able to drive CXCR3-dependent chemotaxis by placing the CM in the lower chambers of our transwell system (Fig. 5E). The chemotactic index of both the CD4+ T cells and CD8+ T cells was significantly increased in response to the TNF-α-CM (Fig. 5F - G). The chemotactic response was blocked by pre-treating the cells with the CXCR3 antagonist. In addition to chemokines released by HPCs, we investigated if chemokines released by differentiated HPCs in response to treatment with chronic TNF-α could drive T cell CXCR3-dependent chemotaxis (Fig. 5H- I).

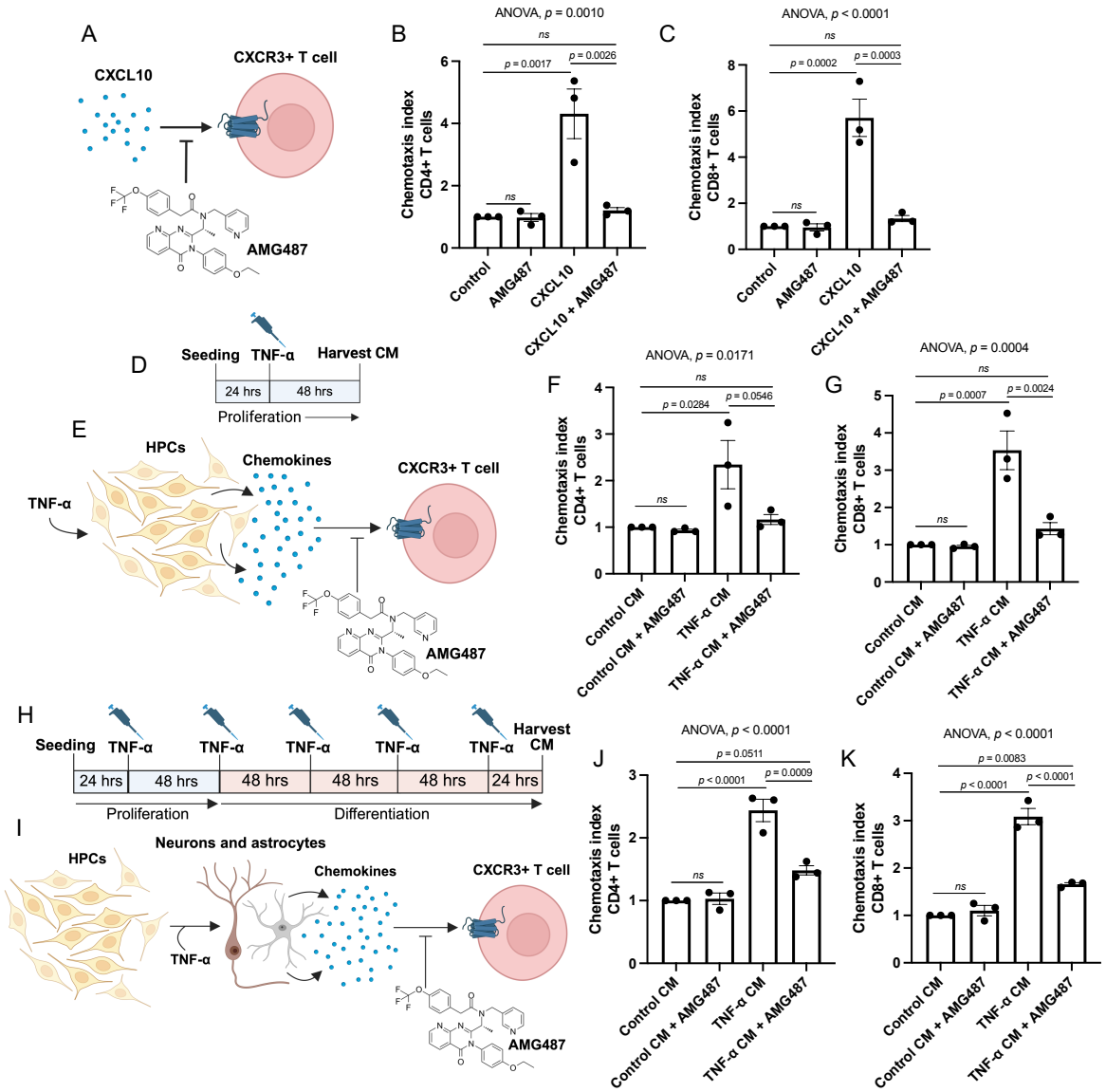

Fig. 5 | TNF-α-conditioned media from proliferating and differentiating HPCs drive CXCR3-dependent chemotaxis of primary, human T cells. A CXCL10 drives T cell chemotaxis by activating CXCR3. AMG487 is a selective CXCR3 antagonist. **B** and **C** Quantification of the chemotactic response (chemotaxis index) of **B** CD4+ T cells and **C** CD8+ T cells treated ± 1 μM AMG487 or DMSO in response to control media or media containing 100 ng/ml recombinant hCXCL10. The chemotactic index is the ratio of the number of cells migrated in response to a stimulus, as compared with controls. Data is represented as mean ± SEM of three healthy donors. Statistical analysis: one-way ANOVA followed by Bonferroni's multiple comparisons test. **D** Schematic overview of the experimental design for generating conditioned media (CM) from HPCs treated for ± 1 ng/ml TNF-α for 48 hrs. **E** We probed if chemokines secreted by HPCs in response to TNF-α could drive CXCR3-dependent T cell chemotaxis. **F** and **G** Quantification of the chemotactic response (chemotaxis index) of **F** CD4+ T cells and **G** CD8+ T cells treated ± 1 μM AMG487 or DMSO in response to control CM or TNF-α-CM from HPCs. Data is represented as mean ± SEM of three healthy donors. Statistical analysis: one-way ANOVA followed by Bonferroni's multiple comparisons test. **H** Schematic overview of the experimental design for generating CM from differentiated HPCs treated chronically ± 1 ng/ml TNF-α. **I** We probed if chemokines secreted by differentiated HPCs in response to chronic TNF-α could drive CXCR3-dependent T cell chemotaxis. **J** and **K** Quantification of the chemotactic response (chemotaxis index) of **J** CD4+ T cells and **K** CD8+ T cells treated ± 1 μM AMG487 or DMSO in response to control CM or TNF-α-CM from differentiated HPCs. Data is represented as mean ± SEM of three healthy donors. Statistical analysis: one-way ANOVA followed by Bonferroni's multiple comparisons test.

Similarly, we found that chemokines released from the HPCs differentiated in the presence of chronic TNF-α drove the CXCR3-dependent chemotaxis of both CD4+ T cells and CD8+ T cells (Fig. 5J-K). In addition to chemokines released by HPCs, we investigated if chemokines released by differentiated HPCs in response to treatment with chronic TNF-α could drive T cell CXCR3-dependent chemotaxis (Fig. 5H- I). Similarly, we found that chemokines released from the HPCs differentiated in the presence of chronic TNF-α drove the CXCR3-dependent of both CD4+ T cells and CD8+ T cells (Fig. 5J-K).

As our data indicated that the CXCL10 upregulation was mediated via the autocrine/paracrine signalling loop, we asked if interfering with the TNF-α-NF-kB-IFN-β-IFNAR-STAT1/2 signalling axis could abrogate the chemotaxis of T cells towards chemokines secreted from TNF-α-treated HPCs. We tested two approaches to interfering with the signalling axis: IFNAR antagonism using anifrolumab and JAK activity antagonism using JAK Inhibitor I (Fig. 6A – B). As already demonstrated, the TNF-α-CM from HPCs drove the chemotaxis of CD4+ T cells and CD8+ T cells, however not when the HPCs were co-treated with anifrolumab or JAK Inhibitor I (Fig. 6C - D). This finding highlighted that secretion of CXCR3-activating chemokines from HPCs in response to TNF-α was dependent on the autocrine/paracrine signalling loop.

Collectively, these data demonstrated that chemokines secreted by HPCs and their differentiated progeny in response to TNF-α can drive the CXCR3-dependent chemotaxis of primary human T cells *in vitro*. Furthermore, the data demonstrated that IFNAR and

JAK antagonism could abrogate the chemotaxis response of T cells towards chemokines released by TNF-α-treated HPCs.

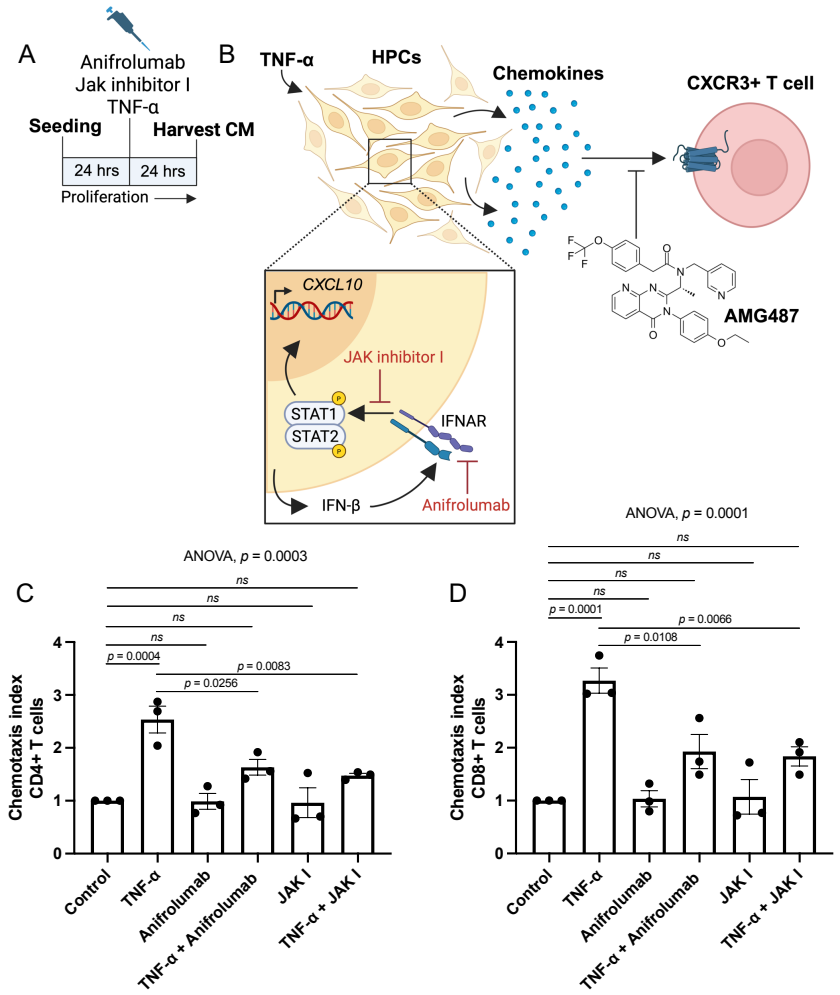

Fig. 6 | JAK and IFNAR signalling are indispensable for TNF-α-induced HPC chemokine secretion directing T cell chemotaxis. **A** Schematic overview of the experimental design for generating conditioned media (CM) from HPCs treated ± 1 ng/ml TNF-α, ± 10 µg/ml anifrolumab (IFNAR antagonist), and ± 0.16 nM JAK inhibitor I for 24 hrs. **B** We probed if interfering with JAK and IFNAR signalling could abrogate the chemotaxis of T cells towards TNF-α-CM from HPCs. **C** and **D** Quantification of the chemotactic response (chemotaxis index) of **C** CD4+ T cells and **D** CD8+ T cells in response to the CM generated as outlined in **A**. Data is represented as mean ± SEM of three healthy donors. Statistical analysis: one-way ANOVA followed by Bonferroni's multiple comparisons test.

IFNAR blockage rescued the chronic TNF-α-induced decrease in the percentage of DCX+ neuroblasts

TNF-α-induced STAT1/STAT2 activation was particularly interesting as STAT1 has been described as negative regulators of hippocampal neurogenesis and associated

cognition[40,58–60]. Therefore, TNF-α-induced STAT1/STAT2 activation could be mediating the antineurogenic effect of TNF-α. To this end, we asked if IFNAR antagonism could abrogate the antineurogenic effect we had previously observed in response to chronic TNF-α. In line with our previous findings, chronic TNF-α treatment did not affect the percentage of MAP2+ cells but led to a significant decrease in the percentage of DCX+ cells (Fig. 7 A-C). However, IFNAR antagonism using anifrolumab rescued the TNF-α-induced decrease in the percentage of DCX+ cells. This finding highlighted that the antineurogenic effect of chronic TNF-α was mediated by the autocrine/paracrine signalling loop and aligns with previous reports of restoring hippocampal neurogenesis by blocking type I signalling in the ageing brain[61.]

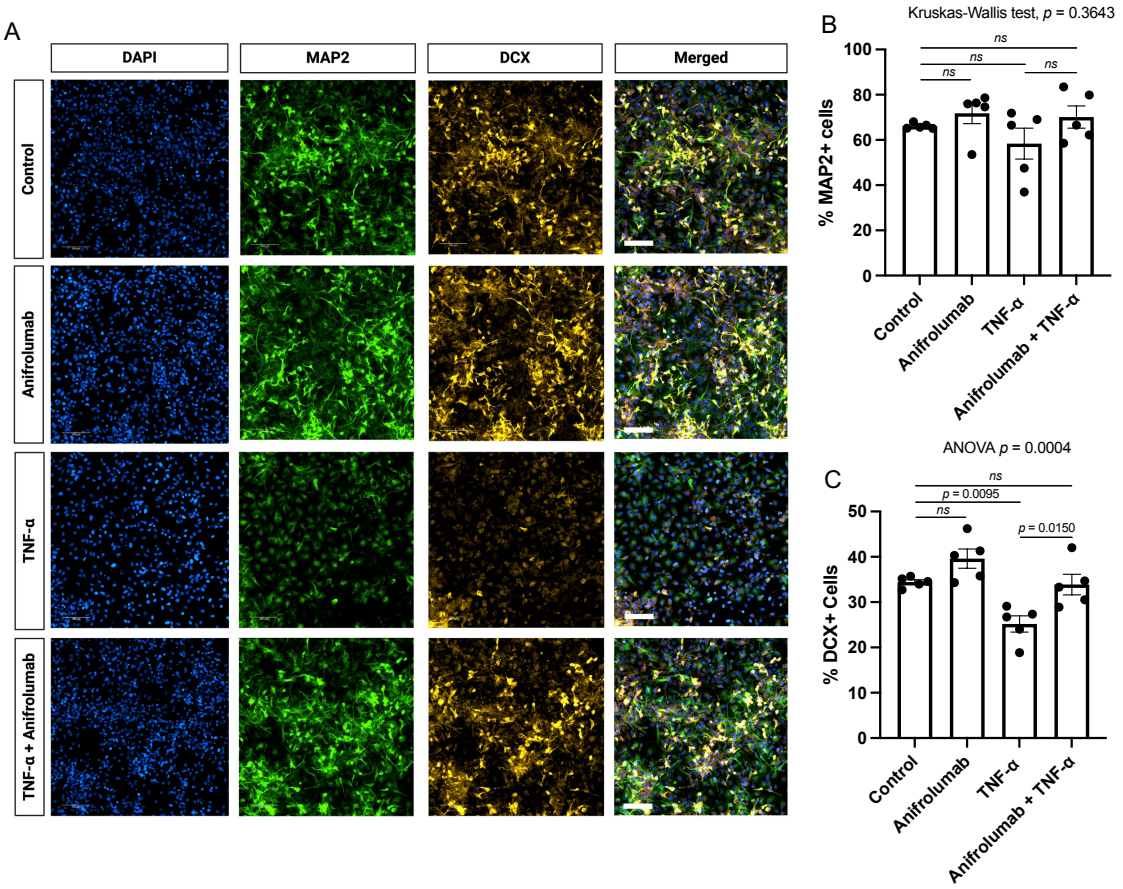

Fig. 7 | IFNAR blockage rescues the chronic TNF-α-induced decrease in the percentage of DCX+ neuroblasts. A Representative images showing the expression of MAP2 (green) and DCX (orange) ion seven days differentiated HPCs treated chronically ± 1 TNF-α ± 10 µg/ml anifrolumab. Scale bar represents 100 µm. **B** and **C** Quantification of the percentage of **B** MAP2+ cells and **C** DCX+ cells respectively based on **A**. Data represent mean ± SEM from five independent experiments. Statistical analysis: **B** Kruskal-Wallis test followed by Dunn's post hoc correction and **C** one-way ANOVA followed by Bonferroni's multiple comparisons test.

Discussion

Emerging evidence has highlighted that ageing and neurodegenerative disease are associated with neuroinflammation, dysfunctional AHN, and accumulation of T cells in the hippocampal neurogenic niche[30–32]. We hypothesised, that chronic TNF-α drives a functional switch in human HPCs away from neurogenesis towards immune response analogously to findings from a recent study of olfactory NSCs[29]. This switch may explain the dysfunctional AHN and infiltration of T cells, which have been suggested to drive cognitive symptoms in ageing and AD mouse models. In this study, we used an *in vitro*

model of human hippocampal neurogenesis to demonstrate that chronic TNF-α changes the cell fate of human HPCs from neurogenesis to immune response. Chronic TNF-α impaired neurogenesis and stimulated CXCL10 secretion. To investigate the molecular mechanisms of how chronic TNF-α changed the behaviours of HPCs we performed scRNAseq and unexpectedly showed that TNF-α drives type I IFN signalling in HPCs. Mechanistically, we showed that TNF-α-induced type I IFN signalling was mediated by autocrine/paracrine IFN-β signalling. The type I IFN signalling loop mediated the secretion of chemokines driving CXCR3-dependent chemotaxis of primary human T cells and the antineurogenic effects of chronic TNF-α. Our data highlight that chronic TNF-α changes the fate of human HPCs from neurogenesis to immune defence via a novel signalling axis not previously described in CNS cell types. We highlight IFNAR antagonism as a dual target for therapeutic intervention blocking the antineurogenic effect of chronic TNF-α and abrogating the chemotaxis of T cells.

The antineurogenic effects of TNF-α we observed recapitulated findings from the study of primary NSCs and animal models[28,62–64]. Similarly, the negative effects of TNF-α on neuronal morphological maturation[64,65] and CXCL10 secretion we observed align with studies of primary cells[66]. The consistency between our findings with those reported in animal models and primary cells supports the physiological relevance of our cellular model. However, investigating if our findings translate to *in vivo* systems will be important.

While type I IFN signalling has been extensively studied in infectious disease[67], its role in sterile inflammation under homeostatic or disease states is less characterised but an

emerging field[68,69]. In the context of sterile inflammation, the cGAS-STING pathway has gained traction as an initiator of type I IFN signalling[70,71]. However, very little is known about the induction of type I IFNs by endogenous inflammatory factors such as cytokines. TNF-α-mediated induction of IFN-β has been described in heart microvasculature endothelial cells[42], fibroblast-like synoviocytes[45], airway smooth muscle cells[72], myeloid cells[43], and various cell lines[73–76]. For several of these cell types, IFN-β upregulation was dependent on IRF1 and NF-κB[42,43,45,72]. IFN-β was subsequently shown to drive autocrine/paracrine signalling via IFNAR and downstream STAT1/2 to drive the expression of CXCR3 chemokines and antiviral genes[42,43,45]. Similarly, we demonstrated that TNF-α drives type I IFN signalling in HPCs via autocrine/paracrine signalling. As the kinetics of the TNF-α-induced upregulation of *IFNB1* correlated with the kinetics of the STAT1 and STAT2 activation IFN-β is the likely mediator of the loop. As demonstrated for other cell types the TNF-α-induced *IFNB1* upregulation was independent of *de novo* protein synthesis but dependent on NF-kB signalling. TNF-α-induced type I IFN signalling mediated via IFNAR has not previously been demonstrated in CNS resident cell types. Investigating if the signalling axis is conserved across other CNS resident cell types such as microglia, astrocytes, and neurons will be an exciting new endeavour. This is particularly relevant for microglia, as IFN-responsive microglia have recently been identified across a broad range of sterile brain pathologies[77]. As IFNAR is ubiquitously expressed[78], type I IFNs secreted from HPCs in response to TNF-α may activate IFNAR neighbouring cells in the neurogenic niche.

From their initial discovery, type I IFNs have mainly been considered beneficial due to their antiviral activities. Additionally, tonic type I IFN signalling plays an important role in maintaining brain homeostasis and cognitive functions[79,80]. However, more recently it has become evident that type I IFNs can be harmful when inappropriately expressed or deregulated[81]. This is emerging to be the case in the ageing brain[61,82] and AD[83–87]. As an example, the top gene contributing to an NSC/NPC chronological ageing clock was the type I IFN-regulated gene *IFI27*[88]. Type I IFNs can induce the expression of IFITM3 on neurons and astrocytes, enhancing γ-secretase activity, thereby promoting the cleavage of APP and increasing amyloid pathology demonstrating their neurotoxic potential[89]. In addition to their molecular and cellular effects, studies have demonstrated that type I IFN signalling play an active role in driving cognitive decline and memory impairment in ageing and AD[61,90–92]. IFNAR blockage delivered by osmotic pumps or intracerebroventricular injection rescues impaired cognition and memory in aged mice and AD mice[61,90]. Intriguingly, the tests used in these studies to assess cognition and memory, the Morris water maze test and the novel location recognition test, are standard tests for hippocampal functioning[14,93]. Furthermore, IFNAR antagonism was found to rescue the number of DCX+ neuroblasts in DG of aged animals[61]. It is therefore likely that the cognitive impairment in ageing and AD mice results from type I IFN-induced AHN dysfunction potentially driven by TNF-α. In support of this hypothesis, we found that the antineurogenic effect of TNF-α was mediated by type I IFN signalling. Type I IFNs mediate their antineurogenic by making NSCs exit the activation state thereby making them less inclined to differentiate[39,94]. Our data adds to the evidence of the antineurogenic effect of

type I IFNs and highlights the therapeutic potential of IFNAR antagonism for preserving AHN in neuroinflammatory conditions.

T cells can infiltrate neurogenic niches in the context of ageing and AD[30–32,49–53,95]. Importantly, growing evidence suggests that peripheral lymphocytes can modulate brain ageing and neuroregeneration by cytokine secretion, plaque clearance, and intercellular communication[96–98]. It is therefore important to understand the mechanisms involved in their infiltration as well as their interactions with brain resident cells. The CXCL10 levels in the supernatant of TNF-α-treated HPCs and differentiated progeny were above 10 ng/ml which has previously been shown to drive significant T cell chemotaxis[99,100]. Therefore, we asked if chemokines secreted from HPCs and their differentiated progeny in response to TNF-α could drive the chemotaxis of primary human T cells. We demonstrated CXCR3-dependent T cell chemotaxis towards chemokines secreted from HPCs in response to TNF-α which raises the possibility that NSC could play a direct role in recruiting T cells into neurogenic niches in a neuroinflammatory context as previously suggested[101]. This finding supported our hypothesis, that TNF-α can switch the HPC phenotype towards one contributing directly to immune recruitment in a similar manner to olfactory NSCs[29]. Our data indicate, that NSCs across species and neurogenic niches share the capacity to directly regulate peripheral immune cell recruitment in the context of chronic TNF-α. In addition to NSCs, microglial activation drives CXCL10-mediated CD8+ T cell recruitment which promotes aging-related white matter degeneration[102]. Hence, multiple cell types likely participate in the recruitment of T cells via the secretion of CXCR3-ligands in ageing and neurodegeneration.

We went on to demonstrate, that IFNAR and JAK activity antagonism abrogated the chemotactic response of T cells towards TNF-α-CM. This finding highlighted, that the autocrine/paracrine type I IFN signalling loop was the main mechanism driving the secretion of CXCR3 ligands. This finding mirrors the discovery that TNFR2-induced IFN-β autocrine signalling *in vivo* promotes renal monocyte recruitment in a nephritis animal model[42]. In addition to the kidneys, type I IFN signalling has been demonstrated to drive immune cell recruitment into the brain. Type I IFN signalling in astrocytes was recently demonstrated to promote brain metastasis by enhancing monocytic myeloid recruitment[103]. Besides driving chemotaxis of T cells, HPC-secreted CXCR3 ligands could have direct deleterious effects on other cell types in the neurogenic niche. CXCR3 is expressed by human microglia, astrocytes, and neurons[86,104] and has been demonstrated to drive hippocampal neural hyperexcitability[86,105,106].

CXCR3 ligands CXCL10 and CXCL11 are upregulated IFN-γ[54]. Therefore, IFN-γ secreted by infiltrating CD8+ T cells could drive further secretion of CXCR3 ligands from NSCs subsequently promoting further CD8+ T cell chemotaxis. This potential positive feedback loop could reinforce the chemotaxis of the CD8+ T cells towards NSCs and explain why CD8+ T cells have been found in close proximity to NSCs[30]. Increasing the number of CD8+ T cells in the hippocampus has been shown to decrease the number of proliferative progenitors and DCX+ newborn neurons[31]. This effect is likely mediated with IFN-γ secretion which has been shown to negatively affect NSCs[30]. Similarly, inhibiting CXCL10 in the SVZ has been found to increase the production of neuroblasts[94], an effect which may be mediated by reduced T cell infiltration. Therefore, TNF-α may negatively regulate

AHN *in vivo* by both driving antineurogenic type I IFN signalling in NSCs, and by driving chemotaxis of CD8+ T cells towards NSCs which subsequently decreases neurogenesis by secreting IFN-γ. Blocking the infiltration of adaptive immune cells into the dentate gyrus may hold therapeutic potential for the treatment of cognitive decline in ageing and neurodegeneration. However, given the relatively low frequency of NSCs, future *in vivo* studies are needed to evaluate if NSCs substantially contribute to the T cell infiltration into neurogenic niches observed in ageing or neurodegeneration.

The TNF-α-induced functional switch we observed in human HPCs from a neurogenic phenotype towards an immune response phenotype may serve as a protective strategy in the face of infection or injury. Generating new neurons is an energetically expensive process, and it might therefore be advantageous to channel the energy usage towards promoting an immune response to resolve the cause of the pro-inflammatory milieu.

Collectively, our results provide significant insight into how chronic TNF-α changes the fate of human HPCs from neurogenesis to immune functions and elucidate the molecular mechanism underlying the switch. Furthermore, it offers a novel explanation for the emerging appearance of type I IFN signalling in ageing and neurodegeneration where TNF-α levels are elevated and highlights HPCs as potential direct participants in the progression of chronic inflammation.

Methods

Cellular model of hippocampal neurogenesis

We used the human hippocampal progenitor cell line (HPC0A07/03A; ReNeuron LTD., Surrey, United Kingdom), derived from a first-trimester female foetus ethically approved under UK and US guidelines, as a cellular model for hippocampal neurogenesis as previously described[107–110]. The cell line was immortalised using the c-*mycER*^{TAM} gene to conditionally proliferate in presence of 100 nM 4-hydroxy-tamoxifen (4-OHT, Sigma Aldrich, #H7904), 10 ng/mL human basic fibroblast growth factor (bFGF, Peprotech, #100-18B-500) and 20 ng/mL human epidermal growth factor (EGF, Peprotech, #AF100-15–500) and spontaneously differentiate in their absence. The cells were cultured as previously described[111] on laminin (Gibco, #23017015) coated culture vessels (Nunclon, Denmark) at 37 °C, 5 % CO2.

TNF-α-treatments

The HPCs were treated with TNF-α (300-01A, Peprotech) for the duration and with the concentrations indicated in the individual experiments.

Immunocytochemistry

Cells were fixed in 4% paraformaldehyde (PFA) in PBS for 15 min at room temperature following PBS washes. For standard ICC, cells were permeabilised and blocked for 1 hr at room temperature in blocking buffer (0.3% Triton X-100, 5% normal donkey serum in PBS). For TNFR1 and TNFR2 staining, a non-permeabilising buffer (5% normal donkey serum in PBS) was used. Primary antibodies (see Table 1) were applied overnight at

4 °C in blocking buffer. The next day, cells were washed 3× with PBS and incubated with appropriate secondary antibodies (see Table 1) in blocking buffer for 2 hr at room temperature, protected from light. After PBS washes, nuclei were counterstained with 300 nM DAPI (Sigma, #62248) for 5 min. Finally, cells were washed 4× with PBS and stored at 4 °C in PBS with 0.05% sodium azide (Merck, #S2002).

Antibody	Manufacturer	Catalogue number	Dilution
Mouse Nestin	Chemicon	Mab5326	1:1000
Mouse MAP2	Abcam	Ab11267	1:500
Rabbit DCX	Abcam	Ab18723	1:500
Mouse STAT1	Cell Signalling Technology	9176	1:1000
Rabbit ISG15	Proteintech	15981-1-AP	1:500
Mouse NF-κB p65	Santa Cruz	Sc-8008	1:500
Donkey anti-rabbit Alexa fluor 555	Invitrogen	A-31571	1:500
Donkey anti-rabbit Alexa fluor 488	Invitrogen	A-21202	1:500

Table 1: Primary and secondary antibodies used for immunocytochemistry.

High-content imaging and analysis

All immunostainings were imaged using the Opera Phenix Plus High-Content Screening System (PerkinElmer) at the Wohl Cellular Imaging Centre. The cells were imaged in a single focal plane with a 20x water immersion lens. A minimum of 9 fields were imaged per well in the 96 well plates and the measures were averaged across the fields to get a mean per well. The cells were imaged using the following channels detected with excitation (ex) laser/emission filters (em): DAPI $ex_{385nm}/em_{425-475nm}$; AlexaFluor™488

$ex_{488nm}/em_{500nm-550nm}$; AlexaFluor™555 $ex_{561}/em_{609nm-644nm}$. A minimum of three technical wells were imaged per marker and were averaged for each biological replicate.

The high-content imaging and analysis software Harmony (PerkinElmer) was used to analyse the imaging data. Images were analysed with custom-built analysis sequences based on predefined analysis building blocks. The setting for each building block was adjusted at each step. Briefly, the cells were identified using the Find Nuclei building block. The Calculate Morphological Properties building block was included to get morphology parameters on each cell. Nuclei smaller than 50 μm^2 or larger than 500 μm^2 were filtered out to remove apoptotic bodies and DAPI artefacts. An additional step was included to remove cells on the border of each field from the downstream analysis. The Find Cytoplasm, Find Morphological Properties, and Calculate Intensity Properties building blocks were included to identify the staining signal intensity in the cytoplasm or the nucleus. Positive cells were then selected with the Select Population building block by setting a minimum intensity threshold for each plate based on visual inspection of the control wells. The percentage of positive cells for a given marker was calculated with the Define Results building block by dividing the number of positive cells by the total number of cells and multiplying by 100. The data were then exported from Harmony and analysed in GraphPad Prism.

RNA extraction, cDNA synthesis, and RT-qPCR

Cell lysis and RNA extraction

3.5×10^5 HPCs were seeded per well in 6-well plates coated with 20 µg/mL mouse laminin (Sigma, #L2020). The following day, cells were treated as required. For lysis,

media were removed and wells washed with PBS. Cells were lysed in 350 µL Buffer RLT Plus (Qiagen, #74134) supplemented with 2-mercaptoethanol (1:100, Bio-Rad, #1610710), then scraped, transferred to Eppendorf tubes, vortexed, and stored at –80 °C. Total RNA was extracted using the RNeasy Plus Mini Kit (Qiagen, #74134) according to the manufacturer's instructions, and concentrations were measured using a NanoDrop spectrophotometer (Thermo Fisher Scientific).

cDNA synthesis

200 ng extracted RNA was reverse transcribed into cDNA using the High-Capacity cDNA Reverse Transcription Kit (4368813, Applied Biosystems) according to the manufacturer's protocol. The protocol employed on the thermal cycler (Biometra Trio series, Analytic Jeka) for the cDNA synthesis has been outlined in Table 2.

Step	Temperature (°C)	Time (minutes)
1	25	10
2	37	120
3	85	5
4	4	∞

Table 2: Thermal cycler program employed for cDNA synthesis.

RT-qPCR

5 µL of cDNA (diluted 1:4 in nuclease-free water) was used per reaction with 10 µL SYBR Green Master Mix (PCR Biosystems, #PB20.11-05), 4 µL nuclease-free water, and 1 µL of primer mix (10 pmol). Reactions were run in triplicate in 384-well plates (Applied

Biosystems, #4309849) using a QuantStudio 5 Real-Time PCR System (Applied Biosystems) and the cycling program detailed in Table 3. Data were analysed using QuantStudio Design & Analysis Software (v1.5.1). Relative gene expression was calculated via the 2^–ΔΔCt method, normalising to GAPDH. Primer sequences are listed in Table 4.

Step	Temperature (°C)	Time
1	50	2 minutes
2	95	10 minutes
3 (40 cycles)	95	15 seconds
4 (40 cycles)	60	1 minute
5	95	15 seconds

Table 3: Thermal cycling conditions employed for RT-qPCR

Gene	Sequence
CD70	Forward: 5'-TTCGCACAGGCTCAGCAGCAG-3' Reverse: 5'-TTGTCCAGCTCTGGTCCATGCA-3'
CEACAM1	Forward: 5'-CACGCCAATAACTCAGTCACTGG-3' Reverse: 5'-TTGTGGAGCAGGTCAGGTTCAC-3'
CXCL10	Forward: 5'-GGTGAGAAGAGATGTCTGAATCC-3' Reverse: 5'-GTCCATCCTTGGAAGCACTGCA-3'
GAPDH	Forward: 5'-GTCTCCTCTGACTTCAACAGCG-3' Reverse: 5'-ACCACCCTGTTGCTGTAGCCAA-3'
ICAM1	Forward: 5'-AGCGGCTGACGTGTGCAGTAAT-3' Reverse: 5'-TCTGAGACCTCTGGCTTCGTCA-3'
IFNB1	Forward: 5'-CTTGGATTCCTACAAAGAAGCAGC-3'

	Reverse: 5'-TCCTCCTTCTGGAACTGCTGCA-3'
IRF1	Forward: 5'-GAGGAGGTGAAAGACCAGAGCA-3' Reverse: 5'-TAGCATCTCGGCTGGACTTCGA-3'
LGALS9	Forward: 5'-ACACCCAGATCGACAACTCCTG-3' Reverse: 5'-CAAACAGGTGCTGACCATCCAC-3'
NECTIN2	Forward: 5'-GAGCAGATGGTGTCACGGTCAC-3' Reverse: 5'-GAGATGGACACTTCAGGAGGGT-3'
VCAM1	Forward: 5'-GATTCTGTGCCCACAGTAAGGC-3' Reverse: 5'-TGGTCACAGAGCCACCTTCTTG-3'

Table 4: Primers used for RT-qPCR

Western blotting

3–6 × 10^5 HPCs were seeded into laminin-coated 6-well plates (Thermo Fisher, #140675). Cells were harvested by PBS wash and lysed in 150 µL 1× Laemmli buffer (Bio-Rad, #1610747) diluted in PBS and supplemented with 355 mM β-mercaptoethanol (Bio-Rad, #1610710). Lysates were scraped, boiled for 5 min at 95 °C, and stored at –80 °C. Proteins were separated via 10% SDS-PAGE and transferred to PVDF membranes (Thermo Fisher, #88518). Membranes were blocked for 1 hr at room temperature with 5% milk in PBS + 0.1% Tween-20, then washed 3× with PBS + 0.5% Tween-20 (10 min each). Primary antibodies (Table 5) were applied overnight at 4 °C in the same blocking buffer. After washing, membranes were incubated with HRP-conjugated secondary antibodies for 1 hr at room temperature, followed by another 3× wash with PBS + 0.5% Tween. Signal detection was performed using Clarity Max ECL Substrate (Bio-Rad, #1705062) for STAT proteins and Clarity ECL Substrate (Bio-Rad, #1705061) for GAPDH (each for 4 min), and imaged with the ImageQuant 800 Imager (Amersham). Band intensities were quantified using Image Studio.

Target	Company	Catalogue number	Species	Concentration
p-STAT1	Cell Signalling Technology	91715	Rabbit	1:1000
p-STAT2	Cell Signalling Technology	88410	Rabbit	1:1000
GAPDH	Proteintech	60004-1-1g	Mouse	1:10000
STAT1	Cell Signalling Technology	9176	Mouse	1:1000
STAT2	Cell Signalling Technology	71604	Rabbit	1:1000
Anti-rabbit	GE	NA9340V	Donkey	1:3000
Anti- mouse	Santa Cruz Biotechnology	D1321	Goat	1:9000

Table 5: Antibodies used for western blot experiments.

Western blotting quantifications

Band intensities for phosphorylated STAT proteins, total STAT proteins, and GAPDH (loading control) were quantified. Phospho- and total STAT signals were normalised to GAPDH, with GAPDH intensity first normalised across samples. Fold changes in phosphorylated STAT levels relative to total STAT were then calculated and expressed relative to the control condition.

Statistical analysis

Statistical analyses were performed using GraphPad Prism (v10.4.1) and R (v4.3.2) with the rstatix package (v0.7.2). Normality was assessed by visual inspection of Q–Q plots and the Shapiro–Wilk test, while homogeneity of variance between groups was evaluated

using Levene's test. Data are presented as mean ± standard error of the mean (SEM), and a p-value of < 0.05 was considered statistically significant. The specific statistical test used and the sample size for each experiment are reported in the corresponding figure legend. If data were normally distributed ($p > 0.05$), parametric tests were applied: comparisons between two groups were made using an unpaired Student's t-test, and comparisons among more than two groups were analysed using one-way ANOVA followed by Bonferroni's multiple comparisons test. In cases of unequal variance, a t-test with Welch's correction or a Welch ANOVA followed by the Games–Howell post hoc test was used. For non-normally distributed data ($p < 0.05$), non-parametric tests were used: the Wilcoxon rank-sum test for two-group comparisons, and the Kruskal–Wallis test with Dunn's post hoc test for comparisons involving more than two groups.

NF-kB nuclear translocation assay

HPCs were seeded on laminin-coated 96-well plates at a density of 1.2×10^4 cells per well. After culturing the cells for 24 hours in proliferation media, the media was replaced with proliferation media ± 10 ng/mL TNF-α. The cells were fixed at baseline and after 15 minutes, 30 minutes, 45 minutes, 60 minutes, 2 hours, 3 hours, 4 hours, 24 hours, and 48 hours of treatment. The cells were immunoassayed for NF-κB p65 (cs-8008, Santa Cruz) and DAPI as described elsewhere. High-content imaging was performed on Opera Phenix (Perkin Elmer). The cellular imaging software Harmony (PerkinElmer) was used to quantify the nuclear translocation of NF-kB p65. Briefly, the DAPI stain was used to identify the nuclei and the Alexa Fluor 488 conjugated NF-κB p65 antibody for identifying the cytoplasm. The intensity of the NF-kB p65 signal in the cytoplasm and nucleus was calculated and the fraction of nuclear fluorescence was calculated as shown below:

$$Fraction\ of\ nuclear\ fluorescence = \frac{Nuclear\ intensity}{Nuclear\ intensity + cytosol\ intensity}$$

Cytokine and chemokine secretion analysis

1.2 x 10^5 HPCs were seeded into 24-well plates (142475, Thermo Fisher Scientific) coated with 20 µg/ml mouse laminin (L2020, Sigma). After 24 hours of culturing in proliferation media, the media was changed to proliferation media ± TNF-α. After 24 hours and 48 hours of treatment in proliferation media, the supernatant was harvested. After 48 hours of treatment in proliferation media, the cells were washed twice in 30 minutes in differentiation media. The media was then changed to differentiation media ± TNF-α. The supernatant was then harvested after 24 hours, 48 hours, and 7 days of differentiation ± TNF-α. The supernatants were frozen down at -80°C until analysed. The concentration of IL-6 in the supernatant was analysed using an IL-6 sandwich enzyme-linked immunosorbent assay (ELISA) (430504, Biolegend) according to the manufacturer's instructions. The concentration of a panel of human pro-inflammatory chemokines (listed in Table 6) was analysed using a multiplex bead-based assay kit (740985, Biolegend) according to the manufacturer's instructions. The samples were run on a FACSCanto II (BD Biosciences) flow cytometer, and the data were analysed using the LEGENDplex data analysis software suite (Biolegend).

Chemokine	Full name	Alias
CCL2	Chemokine (CC motif) ligand 2	MCP-1
CCL3	Chemokine (CC motif) ligand 3	MIP-1α
CCL4	Chemokine (CC motif) ligand 4	MIP-1β
CXCL1	Chemokine (CXC motif) ligand 1	GROα

CXCL5	Chemokine (CXC motif) ligand 5	ENA-78
CXCL8	Chemokine (CXC motif) ligand 8	IL-8
CXCL9	Chemokine (CXC motif) ligand 9	MIG
CXCL10	Chemokine (CXC motif) ligand 10	IP-10
CXCL11	Chemokine (CXC motif) ligand 11	I-TAC
CCL11	Chemokine (CC motif) ligand 11	Eotaxin
CCL17	Chemokine (CC motif) ligand 17	TARC
CCL20	Chemokine (CC motif) ligand 20	MIP-3α

Table 5: Chemokines included in the human pro-inflammatory chemokine panel.

Differentiation assay for immunocytochemistry

HPCs were seeded on laminin-coated 96-well plates at a density of 1.2 x 10^4 cells per well in three technical replicates. After culturing the cells for 24 hours in proliferation media (containing 4-OHT, bFGF, and EGF), the media was replaced with proliferation media ± TNF-α. After 48 hours in proliferation media, the cells were washed twice in differentiation media (no 4-OHT, no bFGF, and no EGF) for 30 minutes. The media was then changed to differentiation media ± TNF-α. The cells were then cultured in differentiation media for seven days where the media was replaced every 48 hours ± TNF-α. In a second round of experiments probing the effect of IFNAR blockage, the cells were cultured as described above but treated ± 1 ng/ml TNF-α and ± 10 µg/ml anifrolumab.

Neurite outgrowth analysis

The neurite outgrowth analysis of DCX+ and MAP2+ cell populations was performed using the high-content imaging and analysis software Harmony (PerkinElmer). DCX+ and MAP2+ cell populations were identified as described in the section on high-content

imaging and analysis. The building block 'Find Neurites' was used to identify neurites. A set of numerical properties, characterising each cell's neurite tree, was calculated including the length of the longest neurite.

Cell culture and treatment for the single-cell RNA sequencing

Proliferating HPCs

For the control cells and cells treated with low TNF-α (0.1 ng/mL) 2.9 x 10^6 cells were seeded into a 20 µg/ml mouse laminin (L2020, Sigma) coated T175 flask. For the cells treated with high TNF-α (1 ng/mL) 5 x 10^6 cells were seeded into a 20 µg/ml mouse laminin (L2020, Sigma) coated T175 flask. The day after seeding, the media was changed to proliferation media ± 0.1 ng/ml TNF-α or 1 ng/ml TNF-α. After 48 hours of proliferation, the cells were harvested. The three proliferation samples were harvested at the same time to minimise the batch effect.

Differentiated HPCs

For the control cells and cells treated with low TNF-α (0.1 ng/mL) 2.9 x 10^6 cells were seeded into a 20 µg/ml mouse laminin (L2020, Sigma) coated T175 flask. For the cells treated with high TNF-α (1 ng/mL) 5 x 10^6 cells were seeded into a 20 µg/ml mouse laminin (L2020, Sigma) coated T175 flask. The day after seeding, the media was changed to proliferation media ± 0.1 ng/ml TNF-α or 1 ng/ml TNF-α. After 48 hours of proliferation, the media was changed to differentiation media ± 0.1 ng/ml TNF-α or 1 ng/ml TNF-α. The HPCs were allowed to differentiate for seven or fourteen days. To mimic a chronic TNF-α-mediated proinflammatory environment the differentiation media was changed every 48

hours to fresh differentiation media ± 0.1 ng/ml TNF-α or 1 ng/ml TNF-α. After seven or fourteen days of culturing in differentiation media, the cells were harvested. The culture of the six differentiation samples was staggered for them to be harvested at the same time.

Harvesting cells for single-cell RNA sequencing

On the day of harvest, the media was removed, and the cells were washed in pre-warmed D-PBS (14190144, Gibco). To detach the cells, they were incubated with pre-warmed Accutase (A1110501, Gibco) at 37°C, 5% CO_2 for 5-10 minutes. The cells were harvested with pre-wared DMEM/F12 media (21331020, Gibco) and centrifuged at 100 x for 5 minutes. The cell pellets were gently resuspended in 1 ml warm proliferation or differentiation media. The viability of the samples was confirmed to be ≥ 85% viability before continuing to antibody labelling using a hemocytometer and Trypan Blue (15250061, Thermo Fisher Scientific).

Cell surface staining with hashtag oligonucleotide antibodies

To enable multiplexing of samples for 3' scRNA sequencing on the 10X genomics chromium system we utilised hashtag-oligonucleotide (HTO) TotalSeq™B anti-human antibodies (hashtag 1: 394631, hashtag 2: 394633, hashtag 3: 394635, BioLegend). These antibodies target the ubiquitously expressed cell surface proteins CD298 and beta-2 microglobulin (B2M) on human cells and are conjugated to different oligonucleotide sequences called hashtags. Multiplexing samples using these reagents is referred to as cell hashing and links the transcriptome of each cell with its antibody oligonucleotide 'hashtag' sequence. This protocol allows sample identification from a mixed pool of HTO-

labelled cells. The optimal antibody concentrations were identified by titrating clonally-equivalent PE-conjugated anti-B2M (316305, BioLegend) and anti-CD298 (341704, BioLegend) antibodies mixed in a 1:1 equimolar ratio to mimic the TotalSeqB product formulation and performing ICC. We chose the antibody dilution 1:5000 (125 ng/ml) which labelled 100% of the HPCs and displayed minimum non-specific and background staining. The samples were labelled individually with the three hashtag antibodies before being pooled at the sequencing facility.

For HTO staining, 1 x 10^6 cells from each sample were spun down at 300 x *g* for 5 minutes at 4°C in 1.5 ml polypropylene microcentrifuge tubes. For each sample, the supernatant was removed, and the pellet was resuspended in 45 µl cell staining buffer (CSB) (420201, BioLegend). 5 µl Human TruStain FcXTM (Fc Receptor Blocking Solution) (422301, BioLegend) was added, and the samples were gently mixed by pipetting. The samples were blocked for 10 minutes at 4°C. During blocking, the TotalSeqB antibodies were spun down at 14,000 x *g* for 10 minutes at 4°C. The antibody staining solutions were prepared by diluting the HTO antibodies 1:2500 in the CSB. The antibodies diluted in CSB were mixed 1:1 with the Fc-blocked cells reaching a final antibody concentration of 1:5000. The cells were incubated for 30 minutes at 4°C. Cells were washed by adding CSB to reach 1.5 ml and centrifugating for 5 minutes at 300 x *g* at 4°C. The supernatant was carefully removed, and the pellet was resuspended in 1.5 ml CSB with wide-bore pipette tips (E1011-9618, Starlab). The wash step was repeated twice. Estimating a 50% loss of cells from the starting amount, CSB was added to reach a final cell concentration between 700 – 1,200 cells/µl. The cells were gently mixed to obtain a homogenous single-cell suspension and were filtered through a 40 µm FlowmiTM Cell Strainer (H13680-0040,

Bel-Art, H-B Instrument) to remove cellular debris. By the end of the harvest and staining protocol, the viability of all samples was confirmed to be above 80%. The samples were kept on ice at all times during the protocol before swiftly moving to the 10x workflow.

Single-cell capture, cDNA library preparation, and sequencing

Single-cell capture, library preparation, sequencing, and read alignment were performed by the Genomics Research Platform based at Guy's and St Thomas's Hospital, London, UK. Briefly, HTO-labelled samples were combined into 4 pools. The differentiation samples (three pools) and the proliferation samples (one pool) were delivered to the facility on separate days. Equal numbers of cells were pooled, and 18,000 cells from each pool were loaded onto separate lanes of the microfluidic 10X chip. Each lane/pool was an independent droplet-based capture reaction on the 10x Chromium X instrument (10x Genomics). cDNA library preparation was performed using the Chromium Single Cell 3' Reagent Kit v3 (PN-1000268, 10x Genomics) according to the manufacturer's instructions. The libraries were sequenced on a NextSeq 2000 (Illumina) with 50 base-pair, paired-end reads.

Read alignment and sample demultiplexing

Reads were aligned using 10x Genomics Cell Ranger v. 7.1. The sequencing facility ran the cellranger multi pipeline which takes FASTQ files from gene expression (RNA) and HTO libraries generated per pool. It performs alignment, filtering, barcode counting, and UMI counting. It uses the Chromium cellular barcodes to generate gene expression barcode matrices. The data was run into R/R Studio with the Seurat v5 function read10X(). This function returns a list of matrices: a UMI count (RNA) matrix containing

the number of molecules for each feature (gene) detected in each cell and an HTO count matrix. Cell barcodes detected in both the RNA count matrix and HTO count matrix were filtered and used to subset the RNA counts and HTO counts by joint cell barcodes. A Seurat object was generated by passing the RNA counts to the function CreateSeuratObject(). The HTO counts were added to the Seurat object using the function CreateAssayObject(). The HTO data was normalised with centred log-ratio transformation. The pooled samples were then demultiplexed with the function HTODemux(assay = 'HTO'). For this, default settings were used, and only singlet cells with an identified HTO identity were retained for further analysis. Only singlets were retained for downstream analysis.

Quality control

We performed quality control (QC) at two levels: gene level and cell level. QC was performed in parallel on a merged Seurat object containing all the differentiation samples and a separate Seurat object containing the proliferation samples.

Cell-level filtering

Standard QC plots were generated to assess QC. We calculated the percentage of mitochondrial genes for each cell and filtered out cells with more than 15% mitochondrial genes. We calculated the novelty/complexity score by calculating the log10 transformed number of genes per total number of molecules detected within a cell. We filtered out cells with a novelty score below 0.8 which are considered poor-quality cells. Additionally, we removed cells that expressed with less than 800 genes and more than 8000. Finally, we removed cells with less than 1000 transcripts detected and more than 45,000

transcripts detected. This left a total of 22,133 cells consisting of 15,053 differentiated cells and 7080 proliferating cells.

Gene-level filtering

We removed all genes that were not expressed in any cells and kept only genes that were expressed in more than five cells. After QC 26,288 genes were retained in the differentiation Seurat object, and 21,951 genes were retained in the proliferation Seurat object.

Normalisation, dimensionality reduction, and clustering

We ran the analysis pipeline without integration and found that the data aligned with that from another scRNA sequencing experiment from our lab, which used the same cell line and time points as this project. This other dataset however consisted of one single experimental batch and therefore we expected it to have minimal batch effect. Therefore, we decided not to integrate, as integration itself can introduce errors as it cannot discriminate between biological and technical noise. Therefore, prior to normalisation, the differentiation and proliferation Seurat objects were merged rather than integrated. Normalisation and variance stabilisation of the data was performed using the function sctransform version 2 from Seurat[112]. Following, principal component analysis (PCA) was performed on the normalised data via the function RunPCA() using the top 3000 highly variable genes. The number of PCs explaining much of the data variance was explored by plotting the standard deviation against PC dimensions via the function ElbowPlot(). After PC 50 the standard deviation did not decrease further, and therefore this number of PCs was selected for further analysis, as it explained all variance in the dataset. The

function FindNeighbors() was used to find the nearest neighbours of the single cell data point within the dataset. Clustering was performed with the function FindClusters() using a range of cluster resolutions from 0.1 – 1.2 in 0.1 increments. Non-linear dimensional reduction was performed in PCA space using Uniform Manifold Approximation and Projection (UMAP) with the function RunUMAP() using dims = 1:50. Data was visualised in two-dimensional UMAP space with the function DimPlot(reduction = 'umap').

Cluster annotation

The strategy, to define the number of clusters in the dataset, was to initially over-cluster with a high resolution. Then, clusters were merged if their top cluster markers were not distinct, the clusters were not biologically meaningful, and the clusters shared multiple canonical markers. This was an iterative process of clustering, merging, and re-clustering while evaluating marker gene expression. To find cluster markers we used the function FindAllMarkers() on the normalised data which calculates differential expression (DE) using the Wilcoxon test by comparing the average gene expression in a cluster to all other clusters. Specifically, marker genes should be expressed in a minimum of 25% of cells in the cluster and show positive DE (be a positive marker gene) with a $\log_2$ fold change of a minimum of 0.25. We ended up with 15 clusters which were annotated based on culture condition, treatment condition, cell cycle stage, and expression of canonical marker genes.

Functional enrichment analysis

Functional enrichment analysis was performed using ClusterProfiler[113]. GO over-representation analysis was performed using the top 100 differentially expressed genes based on log fold-change of the average expression between the clusters being compared. The p-value cutoff for raw (unadjusted) p-values was 0.05. We used Benjamin-Hochberg to adjust p-values after conducting GO enrichment analysis with the adjusted p-value cutoff of 0.2 (default).

Transcription factor activity inference

Transcription factor activity analysis was performed using decoupleR package version 2.8[114]. First, CollecTRI[115] was retrieved via OmnipathR[116]. A TF enrichment score was generated using the univariate linear model method. The model fits a linear model for each cell and each TF that predicts the observed gene expression based on only the TF's TE-gene interaction weights. The obtained t-value of the slope fitted is the score. Positive scores indicate that the TF is active, and oppositely a negative score indicates that it is inactive.

Cell cycle analysis

Cell cycle scoring was performed using the Seurat function CellCycleScoring(). This function calculates cell cycle phase scores based on canonical markers of the G2/M and S phases and saves them in the metadata. The S score and G2/M score were visualised on a UMAP plot with the function FeaturePlot().

Gene module scoring for NSC-specific type I IFN response signature

The cells were scored against a 300 gene NSC-specific type I IFN response signature developed by treating murine NSCs from the SVZ *ex vivo* with IFN-β[39]. The average expression of the gene set was calculated for each cell adjusting for background expression using the AddModuleScore().

Gene module scoring for human immature dentate granule cell signature

The cells were scored against the top 20 genes of a gene list used to identify human immature dentate granule cells[9]. The average expression of the gene set was calculated for each cell adjusting for background expression using the AddModuleScore().

Conditioned media experiment for immunocytochemistry

To generate conditioned media (CM) 3 x 10^5 HPCs were seeded into six well plates coated with 20 µg/ml mouse laminin (L2020, Sigma). The following day, the media was changed to fresh media ± 0.1 ng/ml, 1 ng/ml, or 10 ng/ml TNF-α. After 24 hours of treatment, the media was changed to control media and the cells were cultured for another 24 hours without TNF-α, before the CM was harvested. This allowed us to capture HPC-secreted factors in response to TNF-α without residual TNF-α. To evaluate the effect of the CM on the upregulation of the IFN-regulated protein ISG15, other HPCs were seeded into 96 well plates coated with 20 µg/ml mouse laminin (L2020, Sigma). The following day, the media of these cells was changed with a mixture of 70% CM and 30% fresh media. We mixed the CM 70:30 with fresh media to ensure the viability of treated HPCs. After 48 hours of treatment, the cells were fixed, stained with antibodies, and imaged, as described elsewhere, to quantify the percentage of ISG15+ HPCs. The CM was generated from

three independent experiments, and the effect of the CM on the HPCs was evaluated in three independent experiments.

Blocking global protein translation

To investigate the requirement of *de novo* protein synthesis in the TNF-α-induced upregulation of candidate genes, we utilised the global protein translation inhibitor, cycloheximide. The HPCs were treated as described in the results section with 10 µg/ml cycloheximide (01810, Merck).

Blocking NF-kB signalling

To test the role of NF-kB signalling in the TNF-α-induced upregulation of target genes, we used the NF-kB transcriptional activity inhibitor JSH23 (ab144824, Abcam). HPCs were seeded in six wells coated with 20 µg/ml mouse laminin (L2020, Sigma). The following day the media was changed to media with 10 µM JSH23 dissolved in 100% dimethylsulfoxide (DMSO) or DMSO (control). The final concentration of DMSO in both treatment groups was 0.1%. After 30 minutes of pre-treatment ± 1 ng/ml TNF-α was added.

Probing the dependency of IFNAR in TNF-α-induced type I IFN signalling

To probe the dependency of IFNAR in TNF-α-induced type I IFN signalling, we utilised a non-therapeutic biosimilar antibody with the identical variable regions from the therapeutic antibody anifrolumab (SIM0022, Bio X Cell). Anifrolumab binds to IFNAR1 and thereby blocks type I IFN signalling. We used the anti-human IL-6 receptor (tocilizumab biosimilar) (SIM0014, Bio X Cell) as an isotype control antibody, as it has the same immunoglobulin

isotype (IgG1) as the anifrolumab antibody. 1.2 x 10^4 HPCs were seeded in 96-well plates (167008, Thermo Fisher Scientific) coated with 20 µg/ml mouse laminin (L2020, Sigma). The following day they were treated with control media, 10 µg/ml isotype antibody, 10 µg/ml anifrolumab antibody, 1 ng/ml TNF-α, 1 ng/ml TNF-α in combination with 10 µg/ml anifrolumab, or 1 ng/ml TNF-α in combination with 10 µg/ml isotype control antibody. After 24 hours the cells were fixed and stained with DAPI to visualise the cell nucleus, and antibodies visualising ISG15 and STAT1 as described elsewhere. High-content image analysis was used to quantify the percentage of ISG15+ and STAT1+ HPCs as described elsewhere.

Blocking JAK activity

1.2 x 10^4 HPCs were seeded in 96-well plates (167008, Thermo Fisher Scientific) coated with 20 µg/ml mouse laminin (L2020, Sigma). The following day the media was changed to media ± 16 nM of JAK inhibitor I (CAY15146, Cayman Chemical) and ± 1 ng/ml TNF. After 24 hours of treatment, the media was removed, the cells were fixed, and stained before high-content imaging was performed to quantify the percentage of ISG15+ HPCs.

Evaluating cell surface protein expression with flow cytometry

Flow cytometry was performed to evaluate the cell surface expression of adhesion molecules ICAM1, VCAM1, and tetherin on proliferating HPCs. HPCs were grown in T75 flasks coated with 20 µg/ml mouse laminin (L2020, Sigma). The media was changed to fresh media ± 1 ng/ml TNF-α. After 24 hours of treatment, the media was removed, and the cells washed with PBS. The cells were detached using Accutase (A1110501, Sigma) for five minutes in the incubator, harvested, centrifuged, and resuspended in proliferation

media before being transported to the flow cytometry facility on ice. At the facility, the HPCs were centrifuged and resuspended in PBS followed by staining for 15 minutes at RT with Zombie NIR viability dye (423105, BioLegend) at a 1:2000 dilution in PBS. After a subsequent PBS wash, the cells were stained for 40 minutes at 4 °C using the antibodies listed in Table 6 at a 1:100 dilution in staining buffer (PBS + 10 mM HEPES + 2 mM ethylenediaminetetraacetic acid (EDTA) + 0.5% foetal calf serum (FCS)). The cells underwent two further washes with PBS and were resuspended in staining buffer. Data was acquired on a BD FACS Canto II using FACSDiva software version 9.2 (BD Biosciences). Data analysis was performed using FlowJo version 10.10.

Protein	Fluorophore	Company	Catalogue number	Dilution
ICAM1	BV421	Biolegend	353132	1:100
VCAM1	FITC	R&D	BBA22	1:100
Tetherin (BST2)	APC	Biolegend	348410	1:100

Table 6: Antibodies used to analyse cell surface protein expression on HPCs.

Isolating peripheral blood mononuclear cells from leukocyte cones

We isolated primary peripheral blood mononuclear (PBMCs) from leukocyte cones from three healthy donors generated as a by-product of blood donations to the National Health Service Blood and Transplant (NHSBT). Leukocyte cones contain blood enriched for leukocytes. Donors give generic consent for research use as part of the donation process. We acquired the leukocyte cones directly from the Blood and Transplant team in Tooting,

UK, which is part of the NHSBT. PBMC isolation was performed using a standard Ficoll-Paque workflow.

Upon arrival, the cones were carefully cleaned with ethanol before bringing them into a cell culture hood. The cone was placed with the wide side down over a 50 ml centrifuge tube. While holding the cone over the tube, the lower bottom tubing was cut with sterile scissors, leaving a few centimetres of tubing. The cone was left resting on the centrifuge tube and the top tubing was cut. The blood would now start to drip into the tube slowly. However, to ensure efficient transfer from the cone to the tube, an air flush was performed. A sterile 200 µl tip was placed tightly into the top tubing. A blunt-end 19-gauge needle was attached to a 12 ml syringe and used to push air into the 200 µl tip. To rinse the cone, the syringe was filled with 10 ml PBS containing 2% FCS, which was pushed into the 200 µl tip, moving the syringe in a circular motion to wash off the sample from the sides of the cone. The air flush and buffer rinse steps were repeated twice by which point the cone was visually clear and discarded. After recovering the sample from the cone, the centrifuge tube was topped up to 50 ml with PBS containing 2% FCS. The tube was gently mixed by inverting the tube before being centrifuged at 800 x *g* for 10 minutes with the brake on and the deceleration set to high. While spinning, another 50 ml centrifuge tube was prepared containing 15 ml Ficoll-Paque PLUS density gradient media (17144002, Cytiva). After centrifugation the supernatant was carefully removed, and the volume of the cells was mixed 1:1 with Dulbecco's phosphate-buffered saline (DPBS) (14190169, Thermo Fisher Scientific). The volume was mixed well before being carefully layered on top of the 15 ml density gradient media. The 50 ml tube was centrifuged for 30 minutes at 450 x *g* with minimal acceleration and no brake deceleration. After the centrifugation,

the top layer was discarded without disturbing the buffy coat. The buffy coat containing the PBMS was then transferred to a new 50 ml tube and washed by topping the tube up to 50 ml with cold DPBS. The tube was mixed before being centrifuged for 10 minutes at 400 x *g* and 4°C with acceleration and deceleration set to middle level. The supernatant was removed the pellet was resuspended in 25 ml cold DPBS. The tube was centrifuged for 10 minutes at 400 x *g* and 4°C with acceleration and deceleration set to max. The supernatant was discarded again, and the pellet was resuspended in 25 ml cold DPBS. The tube was centrifuged to reduce platelet contamination for 10 minutes at 200 x *g* and 4°C with acceleration and deceleration set to max. The supernatant was discarded, and the pellet was resuspended in 10 ml cold DPBS. At this point, cells were counted while the tube was centrifuged for 10 minutes at 400 x *g* and 4°C with acceleration and deceleration set to max. The supernatant was discarded, and the pellet was resuspended in 1 ml freezing media (90% FBS and 10% DMSO) to obtain 360 – 600 x 10^6 cells/ml. Another 39 ml freezing media was added and mixed well before 1 ml was dispended into 40 cryovials. The cryovials were transferred to a Mr Frosty freezing container and left at -80°C overnight. The following day the cell bank was transferred to storage in liquid nitrogen. For the three donors between 9 – 15 x 10^6 cells were frozen in each cryovial.

Chemotaxis assay

T cell activation and expansion protocol

The PBMC cryovials were thawed in the 37°C water bath. In the cell culture hood, 1 ml Roswell Park Memorial Institute (RPMI) 1640 medium (21875091, Thermo Fisher Scientific) was added to the cryovial and mixed. The mix was transferred to a 15 ml tube which was topped up with PBS and centrifuged at 400 x *g* for 5 minutes. The supernatant

was removed, and the pellet resuspended in 1 ml PBS before topping the tube with PBS. The tube was centrifuged again at 400 x *g* for 5 minutes and the supernatant was removed. The pellet was initially resuspended in 1 ml complete RPMI (supplemented with 10% FCS (26140079, Thermo Fisher Scientific) and 1% penicillin-streptomycin (15140122**,** Thermo Fisher Scientific)) before adding 9 ml complete RPMI and transferring the PBMCs to a T75 cell culture vessel. The cells were cultured at 37 °C and 5% CO_2. The following day the nonadherent cells (primarily consisting of lymphocytes) were harvested into a 15 ml tube. The tube was centrifuged at 400 x *g* for 5 minutes, the supernatant discarded, and the pellet resuspended in 10 ml complete RPMI supplemented with 100 international units (IU)/ml recombinant human IL-2 (689104, Biolegend) and 2.5 µg/ml phytohemagglutinin-L (PHA-L) (00-4977-93, Thermo Fisher Scientific). The cells were transferred to a new T75 tissue culture vessel, now only containing the lymphocytes. After 48 hours of treatment, cells were harvested into a 15 ml tube and centrifuged at 400 x *g* for 5 minutes. The pellet was resuspended in fresh complete RMPI supplemented with 100 (IU)/ml IL-2. The cells were cultured for a total of 10 days and were resuspended in fresh complete RPMI media supplemented with 100 (IU)/ml IL-2 every other day.

Transwell chemotaxis assay

To evaluate the chemotaxis of the activated lymphocytes, we performed transwell migration assays, using high throughput screening (HTS) 96 well transwell plates with 5 µm pores in the polycarbonate membrane separating the upper and lower chamber (#3387, Corning). The day before the assay, the upper wells on the plate were coated with 150 µl 2% bovine serum albumin (BSA) in PBS to minimise lymphocytes sticking to

the plastic during the assay. The plates were left overnight in the incubator. The following morning the wells were washed three times with PBS. The activated lymphocytes were harvested into 15 ml tubes which were topped up with DPBS. The tube was spun down 400 x *g* for 5 minutes and the supernatant discarded. The cells were resuspended in 2 ml migration media (1 ml complete RPMI:9 ml neat RPMI) to study the effect of recombinant chemokine, in HPC proliferation media to study the effect of HPC CM, or in HPC differentiation media to study the effect of CM from differentiating HPCs in chemotaxis. The cells were counted, and the cell concentration was adjusted to 4 -5 x 10^6 cells/ml. If the experiment probed the dependency of the CXCR3 receptor on the cell surface of the activated lymphocytes, the cells were split into two Eppendorf tubes. The CXCR3 antagonist AMG487 (28416, Cayman Chemical), dissolved in 100% DMSO or DMSO for control, was added to the two Eppendorf tubes (the final concentration of AMG487 was 1 μM). After 30 minutes in the incubator with frequent rotations 75 μl of cell suspension were transferred to the upper chambers. To study the effect of recombinant human CXCL10 on chemotaxis, the lower chambers were filled with 235 μl migration media ± 100 ng/ml recombinant human CXCL10 (266-IP, R&D Systems). To study the effect of HPCs secreted factors in response to TNF-α on chemotaxis, the lower chambers were filled with 235 μl ± TNF-α-CM from HPCs. To study the effect of differentiating HPCs secreted factors in response to TNF-α on chemotaxis, the lower chambers were filled with 235 μl ± TNF-α-CM from differentiating cells HPCs. Finally, to evaluate the effect of JAK inhibition and IFNAR blockage in the chemotaxis towards TNF-α-induced secreted chemokines, the lower chambers were filled with 235 μl CM from HPCs treated ± TNF-α, ± JAK inhibitor I, ± anifrolumab. The below section describes the generation of the CM.

After three hours in the incubator, the cells migrated to the lower chamber were harvested and transferred to a round bottom 96 well plate using a multichannel pipet.

Flow cytometry of migrated cells

Flow cytometry was performed to quantify the cells, that had migrated to the lower chamber and evaluate their phenotype. The plate was spun down for 1 minute at 2000 rpm, and the wells were washed with 200 µl DPBS. The plate was spun down for 1 minute at 2000 rpm and the cells were resuspended in Zombie NIR (423105, Biolegend) diluted (1:2000) in DPBS to distinguish live cells. The plate was incubated in the dark for 15 minutes at room temperature. 100 µl DPBS was added to inactive the dye and the cells were spun down 1 minute at 2000 rpm. For experiments evaluating the cell surface expression of CXCR3, an extra step was included where cells were resuspended in 50 µl CXCR3 antibody diluted 1:100 in staining buffer (DPBS+ 10 mM HEPES + 2 mM EDTA + 0.5% FCS). The plate was incubated at 37°C for 15 minutes before a 50 µl antibody master mix of the antibodies listed in Table 7 diluted 1:50 was added. The plate was incubated for 40 minutes at 4°C. The cells were washed with 100 µl staining buffer and spun down for 1 minute at 2000 rpm. They were washed again using 200 µl staining buffer and spun down for 1 minute at 2000 rpm. Finally, the cells were resuspended in 100 µl staining buffer. Data was acquired on a BD FACS Canto II using the high throughput sampler option and FACSDiva software version 9.2 (BD Biosciences). The sample flow rate was set to 3.0, the sample volume to 50 µl, the mixing volume to 50 µl, the mixing speed set to 200, the number of washed was set to 2, and the wash volume set to 200. Data analysis was performed using FlowJo version 10.10.

Protein	Fluorophore	Company	Catalogue number	Dilution
CXCR3	PE	Biolegend	353706	1:100
CD3	BV421	Biolegend	317344	1:100
CD4	PerCP/Cyanine5.5	Biolegend	317428	1:100
CD8	FITC	Biolegend	980908	1:100

Table 7: Antibodies used to analyse cell surface protein expression on immune cells.

Generating conditioned media from HPCs for chemotaxis study

3.5 x 10^5 HPCs were seeded into 6 wells coated with 20 µg/ml mouse laminin (L2020, Sigma). The following day the media was changed to fresh proliferation media ± 1 ng/ml TNF-α. After 48 hours the CM was harvested and centrifuged at 1500 x *g* for 10 minutes at 4°C. The supernatant was harvested to remove cell debris to new tubes and stored at -80°C until used in chemotaxis assays.

Generating conditioned media from differentiating HPCs

3.5 x 10^5 HPCs were seeded into 6 wells coated with 20 µg/ml mouse laminin (L2020, Sigma). The following day the media was changed to fresh proliferation media ± 1 ng/ml TNF-α. After 48 hours the media was changed to differentiation media ± 1 ng/ml TNF-α to induce differentiation. The cells were differentiated for a total of seven days, and every 48 hours the media was changed to fresh differentiation media ± 1 ng/ml TNF-α to mimic chronic inflammation. After seven days of differentiation, the CM was harvested and centrifuged at 1500 x *g* for 10 minutes at 4°C. The supernatant was harvested to remove cell debris to new tubes and stored at -80°C until used in chemotaxis assays.

Generating conditioned media from HPCs blocking JAK activity or IFNAR

3.5 x 10^5 HPCs were seeded into 6 wells coated with 20 µg/ml mouse laminin (#L2020, Sigma). The following day the media was changed to fresh proliferation media with DMSO control, 1 ng/ml TNF-α, 10 µg/ml IFNAR blocking antibody anifrolumab and 1 ng/ml TNF-α, 10 µg/ml IFNAR blocking antibody anifrolumab, 0.15 nM Jak inhibitor I + 1 ng/ml TNF-α, or 0.15 nM Jak inhibitor I. After 24 hours the CM was harvested and centrifuged at 1500 x *g* for 10 minutes at 4°C. The supernatant was harvested to remove cell debris to new tubes and stored at -80°C until used in chemotaxis assays.

Data availability

All source data will be made available via the repository platform *figshare.com* and scripts on *github.com* at the same time as the peer-reviewed publication.

References

1. Ming, G. & Song, H. Adult Neurogenesis in the Mammalian Brain: Significant Answers and Significant Questions. *Neuron* **70**, 687–702 (2011).
2. Altman, J. Autoradiographic investigation of cell proliferation in the brains of rats and cats. *Anat Rec* **145**, 573–591 (1963).
3. Spalding, K. L. *et al.* Dynamics of Hippocampal Neurogenesis in Adult Humans. *Cell* **153**, 1219–1227 (2013).
4. Boldrini, M. *et al.* Human Hippocampal Neurogenesis Persists throughout Aging. *Cell Stem Cell* **22**, 589-599.e5 (2018).
5. Knoth, R. *et al.* Murine features of neurogenesis in the human hippocampus across the lifespan from 0 to 100 years. *PLoS One* **5**, e8809 (2010).
6. Moreno-Jiménez, E. P. *et al.* Adult hippocampal neurogenesis is abundant in neurologically healthy subjects and drops sharply in patients with Alzheimer's disease. *Nat Med* **25**, 554–560 (2019).
7. Tobin, M. K. *et al.* Human Hippocampal Neurogenesis Persists in Aged Adults and Alzheimer's Disease Patients. *Cell Stem Cell* **24**, 974-982.e3 (2019).
8. Palmer, T. D. *et al.* Progenitor cells from human brain after death. *Nature* **411**, 42–43 (2001).
9. Zhou, Y. *et al.* Molecular landscapes of human hippocampal immature neurons across lifespan. *Nature* (2022) doi:10.1038/s41586-022-04912-w.

10. Sorrells, S. F. *et al.* Human hippocampal neurogenesis drops sharply in children to undetectable levels in adults. *Nature* **555**, 377–381 (2018).
11. Sorrells, S. F. *et al.* Positive Controls in Adults and Children Support That Very Few, If Any, New Neurons Are Born in the Adult Human Hippocampus. *The Journal of Neuroscience* **41**, 2554–2565 (2021).
12. Kempermann, G. *et al.* Human Adult Neurogenesis: Evidence and Remaining Questions. *Cell Stem Cell* **23**, 25–30 (2018).
13. Shors, T. J. *et al.* Neurogenesis in the adult is involved in the formation of trace memories. *Nature* **410**, 372–376 (2001).
14. Jessberger, S. *et al.* Dentate gyrus-specific knockdown of adult neurogenesis impairs spatial and object recognition memory in adult rats. *Learning & Memory* **16**, 147–154 (2009).
15. Alonso, M., Petit, A.-C. & Lledo, P.-M. The impact of adult neurogenesis on affective functions: of mice and men. *Mol Psychiatry* **29**, 2527–2542 (2024).
16. Berger, T., Lee, H., Young, A. H., Aarsland, D. & Thuret, S. Adult Hippocampal Neurogenesis in Major Depressive Disorder and Alzheimer's Disease. *Trends Mol Med* **26**, 803–818 (2020).
17. Babcock, K. R., Page, J. S., Fallon, J. R. & Webb, A. E. Adult Hippocampal Neurogenesis in Aging and Alzheimer's Disease. *Stem Cell Reports* **16**, 681–693 (2021).
18. Hill, A. S., Sahay, A. & Hen, R. Increasing Adult Hippocampal Neurogenesis is Sufficient to Reduce Anxiety and Depression-Like Behaviors. *Neuropsychopharmacology* **40**, 2368–2378 (2015).
19. Li, Y.-D. *et al.* Activation of hypothalamic-enhanced adult-born neurons restores cognitive and affective function in Alzheimer's disease. *Cell Stem Cell* **30**, 415-432.e6 (2023).
20. Heneka, M. T. *et al.* Neuroinflammation in Alzheimer disease. *Nat Rev Immunol* **25**, 321–352 (2025).
21. Zhang, W., Sun, H.-S., Wang, X., Dumont, A. S. & Liu, Q. Cellular senescence, DNA damage, and neuroinflammation in the aging brain. *Trends Neurosci* **47**, 461–474 (2024).
22. Beurel, E., Toups, M. & Nemeroff, C. B. The Bidirectional Relationship of Depression and Inflammation: Double Trouble. *Neuron* **107**, 234–256 (2020).
23. Swardfager, W. *et al.* A Meta-Analysis of Cytokines in Alzheimer's Disease. *Biol Psychiatry* **68**, 930–941 (2010).
24. Holmes, C. *et al.* Systemic inflammation and disease progression in Alzheimer disease. *Neurology* **73**, 768–774 (2009).
25. Brymer, K. J., Romay-Tallon, R., Allen, J., Caruncho, H. J. & Kalynchuk, L. E. Exploring the Potential Antidepressant Mechanisms of TNFα Antagonists. *Front Neurosci* **13**, (2019).
26. Enache, D., Pariante, C. M. & Mondelli, V. Markers of central inflammation in major depressive disorder: A systematic review and meta-analysis of studies examining cerebrospinal fluid, positron emission tomography and post-mortem brain tissue. *Brain Behav Immun* **81**, 24–40 (2019).

27. Borsini, A., Zunszain, P. A., Thuret, S. & Pariante, C. M. The role of inflammatory cytokines as key modulators of neurogenesis. *Trends Neurosci* **38**, 145–57 (2015).
28. Monje, M. L., Toda, H. & Palmer, T. D. Inflammatory Blockade Restores Adult Hippocampal Neurogenesis. *Science (1979)* **302**, 1760–1765 (2003).
29. Chen, M., Reed, R. R. & Lane, A. P. Chronic Inflammation Directs an Olfactory Stem Cell Functional Switch from Neuroregeneration to Immune Defense. *Cell Stem Cell* **25**, 501-513.e5 (2019).
30. Dulken, B. W. *et al.* Single-cell analysis reveals T cell infiltration in old neurogenic niches. *Nature* **571**, 205–210 (2019).
31. Wu, Y. *et al.* Multimodal transcriptomics reveal neurogenic aging trajectories and age-related regional inflammation in the dentate gyrus. *Nat Neurosci* **28**, 415–430 (2025).
32. Laurent, C. *et al.* Hippocampal T cell infiltration promotes neuroinflammation and cognitive decline in a mouse model of tauopathy. *Brain* **140**, 184–200 (2017).
33. Kim, M. *et al.* TNF-α induces human neural progenitor cell survival after oxygen–glucose deprivation by activating the NF-κB pathway. *Exp Mol Med* **50**, 1–14 (2018).
34. Abiega, O. *et al.* Hippocampal reactive neural stem cells are able to phagocytose and have an immunological molecular signature. Preprint at https://doi.org/10.1101/2024.01.26.577346 (2024).
35. Llorens-Bobadilla, E. *et al.* Single-Cell Transcriptomics Reveals a Population of Dormant Neural Stem Cells that Become Activated upon Brain Injury. *Cell Stem Cell* **17**, 329–340 (2015).
36. Leeman, D. S. *et al.* Lysosome activation clears aggregates and enhances quiescent neural stem cell activation during aging. *Science (1979)* **359**, 1277–1283 (2018).
37. Belenguer, G. *et al.* Adult Neural Stem Cells Are Alerted by Systemic Inflammation through TNF-α Receptor Signaling. *Cell Stem Cell* **28**, 285-299.e9 (2021).
38. O'Shea, T. M. *et al.* Border-forming wound repair astrocytes. Preprint at https://doi.org/10.1101/2023.08.25.554857 (2023).
39. Carvajal Ibañez, D. *et al.* Interferon regulates neural stem cell function at all ages by orchestrating mTOR and cell cycle. *EMBO Mol Med* **15**, (2023).
40. Borsini, A. *et al.* Interferon-Alpha Reduces Human Hippocampal Neurogenesis and Increases Apoptosis via Activation of Distinct STAT1-Dependent Mechanisms. *Int J Neuropsychopharmacol* **21**, 187–200 (2018).
41. Fujita, T. *et al.* Induction of the transcription factor IRF-1 and interferon-beta mRNAs by cytokines and activators of second-messenger pathways. *Proceedings of the National Academy of Sciences* **86**, 9936–9940 (1989).
42. Venkatesh, D. *et al.* Endothelial TNF Receptor 2 Induces IRF1 Transcription Factor-Dependent Interferon-β Autocrine Signaling to Promote Monocyte Recruitment. *Immunity* **38**, 1025–1037 (2013).
43. Yarilina, A., Park-Min, K.-H., Antoniv, T., Hu, X. & Ivashkiv, L. B. TNF activates an IRF1-dependent autocrine loop leading to sustained expression of chemokines

and STAT1-dependent type I interferon–response genes. *Nat Immunol* **9**, 378–387 (2008).
44. Imanishi, D. *et al.* Identification of a Novel Cytokine Response Element in the Human IFN Regulatory Factor-1 Gene Promoter. *The Journal of Immunology* **165**, 3907–3916 (2000).
45. Bonelli, M. *et al.* IRF1 is critical for the TNF-driven interferon response in rheumatoid fibroblast-like synoviocytes. *Exp Mol Med* **51**, 1–11 (2019).
46. Riggs, J. M. *et al.* Characterisation of anifrolumab, a fully human anti-interferon receptor antagonist antibody for the treatment of systemic lupus erythematosus. *Lupus Sci Med* **5**, e000261 (2018).
47. Thompson, J. E. *et al.* Photochemical preparation of a pyridone containing tetracycle: A jak protein kinase inhibitor. *Bioorg Med Chem Lett* **12**, 1219–1223 (2002).
48. Holmgren, A. M., Miller, K. D., Cavanaugh, S. E. & Rall, G. F. Bst2/Tetherin Is Induced in Neurons by Type I Interferon and Viral Infection but Is Dispensable for Protection against Neurotropic Viral Challenge. *J Virol* **89**, 11011–11018 (2015).
49. Chauquet, S. *et al.* Exercise rejuvenates microglia and reverses T cell accumulation in the aged female mouse brain. *Aging Cell* (2024) doi:10.1111/acel.14172.
50. Krukowski, K. *et al.* Small molecule cognitive enhancer reverses age-related memory decline in mice. *Elife* **9**, (2020).
51. Unger, M. S. *et al.* CD8+ T-cells infiltrate Alzheimer's disease brains and regulate neuronal- and synapse-related gene expression in APP-PS1 transgenic mice. *Brain Behav Immun* **89**, 67–86 (2020).
52. Gate, D. *et al.* Clonally expanded CD8 T cells patrol the cerebrospinal fluid in Alzheimer's disease. *Nature* **577**, 399–404 (2020).
53. Merlini, M., Kirabali, T., Kulic, L., Nitsch, R. M. & Ferretti, M. T. Extravascular CD3+ T Cells in Brains of Alzheimer Disease Patients Correlate with Tau but Not with Amyloid Pathology: An Immunohistochemical Study. *Neurodegener Dis* **18**, 49–56 (2018).
54. Groom, J. R. & Luster, A. D. CXCR3 ligands: redundant, collaborative and antagonistic functions. *Immunol Cell Biol* **89**, 207–215 (2011).
55. Groom, J. R. & Luster, A. D. CXCR3 in T cell function. *Exp Cell Res* **317**, 620–631 (2011).
56. Groh, J. *et al.* Accumulation of cytotoxic T cells in the aged CNS leads to axon degeneration and contributes to cognitive and motor decline. *Nat Aging* **1**, 357–367 (2021).
57. Jiao, H. *et al.* Structure basis for the modulation of CXC chemokine receptor 3 by antagonist AMG487. *Cell Discov* **9**, 119 (2023).
58. Hsu, W.-L., Ma, Y.-L., Hsieh, D.-Y., Liu, Y.-C. & Lee, E. H. STAT1 Negatively Regulates Spatial Memory Formation and Mediates the Memory-Impairing Effect of Aβ. *Neuropsychopharmacology* **39**, 746–758 (2014).
59. Imitola, J. *et al.* Stat1 is an inducible transcriptional repressor of neural stem cells self-renewal program during neuroinflammation. *Front Cell Neurosci* **17**, (2023).
60. Zheng, L.-S. *et al.* Mechanisms for Interferon-α-Induced Depression and Neural Stem Cell Dysfunction. *Stem Cell Reports* **3**, 73–84 (2014).

61. Baruch, K. *et al.* Aging-induced type I interferon response at the choroid plexus negatively affects brain function. *Science (1979)* **346**, 89–93 (2014).
62. Chen, Z. & Palmer, T. D. Differential roles of TNFR1 and TNFR2 signaling in adult hippocampal neurogenesis. *Brain Behav Immun* **30**, 45–53 (2013).
63. Liu, Y.-P., Lin, H.-I. & Tzeng, S.-F. Tumor necrosis factor-α and interleukin-18 modulate neuronal cell fate in embryonic neural progenitor culture. *Brain Res* **1054**, 152–158 (2005).
64. Keohane, A., Ryan, S., Maloney, E., Sullivan, A. M. & Nolan, Y. M. Tumour necrosis factor-α impairs neuronal differentiation but not proliferation of hippocampal neural precursor cells: Role of Hes1. *Molecular and Cellular Neuroscience* **43**, 127–135 (2010).
65. Neumann, H. *et al.* Tumor Necrosis Factor Inhibits Neurite Outgrowth and Branching of Hippocampal Neurons by a Rho-Dependent Mechanism. *The Journal of Neuroscience* **22**, 854–862 (2002).
66. Sheng, W. S. *et al.* TNF-α-induced chemokine production and apoptosis in human neural precursor cells. *J Leukoc Biol* **78**, 1233–1241 (2005).
67. McNab, F., Mayer-Barber, K., Sher, A., Wack, A. & O'Garra, A. Type I interferons in infectious disease. *Nat Rev Immunol* **15**, 87–103 (2015).
68. Ninh, V. K. *et al.* Spatially clustered type I interferon responses at injury borderzones. *Nature* **633**, 174–181 (2024).
69. Ashby, K. M. *et al.* Sterile production of interferons in the thymus affects T cell repertoire selection. *Sci Immunol* **9**, (2024).
70. Couillin, I. & Riteau, N. STING Signaling and Sterile Inflammation. *Front Immunol* **12**, (2021).
71. Gulen, M. F. *et al.* cGAS–STING drives ageing-related inflammation and neurodegeneration. *Nature* **620**, 374–380 (2023).
72. Tliba, O. *et al.* Tumor Necrosis Factor α Modulates Airway Smooth Muscle Function via the Autocrine Action of Interferon β. *Journal of Biological Chemistry* **278**, 50615–50623 (2003).
73. Ahrens, P. B., Besancon, F., Memet, S. & Ankel, H. Tumour Necrosis Factor Enhances induction by beta-Interferon of a Ubiquitin Cross-reactive Protein. *Journal of General Virology* **71**, 1675–1682 (1990).
74. Reis, L. F., Ho Lee, T. & Vilcek, J. Tumor necrosis factor acts synergistically with autocrine interferon-beta and increases interferon-beta mRNA levels in human fibroblasts. *J Biol Chem* **264**, 16351–4 (1989).
75. Hughes, T. K., Kaspar, T. A. & Coppenhaver, D. H. Synergy of antiviral actions of TNF and IFN-γ: Evidence for a major role of TNF-induced IFN-β. *Antiviral Res* **10**, 1–9 (1988).
76. Jacobsen, H., Mestan, J., Mittnacht, S. & Dieffenbach, C. W. Beta interferon subtype 1 induction by tumor necrosis factor. *Mol Cell Biol* **9**, 3037–3042 (1989).
77. Escoubas, C. C. *et al.* Type I interferon responsive microglia shape cortical development and behavior. Preprint at https://doi.org/10.1101/2021.04.29.441889 (2021).
78. de Weerd, N. A. & Nguyen, T. The interferons and their receptors—distribution and regulation. *Immunol Cell Biol* **90**, 483–491 (2012).

79. Cao, W. In sickness and in health—Type I interferon and the brain. *Front Aging Neurosci* **16**, (2024).
80. Hosseini, S. *et al.* Type I Interferon Receptor Signaling in Astrocytes Regulates Hippocampal Synaptic Plasticity and Cognitive Function of the Healthy CNS. *Cell Rep* **31**, 107666 (2020).
81. Georgel, P. Crosstalk between Interleukin-1β and Type I Interferons Signaling in Autoinflammatory Diseases. *Cells* **10**, 1134 (2021).
82. Deczkowska, A. *et al.* Mef2C restrains microglial inflammatory response and is lost in brain ageing in an IFN-I-dependent manner. *Nat Commun* **8**, 717 (2017).
83. Mesquita, S. D. *et al.* The choroid plexus transcriptome reveals changes in type I and II interferon responses in a mouse model of Alzheimer's disease. *Brain Behav Immun* **49**, 280–292 (2015).
84. Roy, E. R. *et al.* Concerted type I interferon signaling in microglia and neural cells promotes memory impairment associated with amyloid β plaques. *Immunity* **55**, 879-894.e6 (2022).
85. Roy, E. R. *et al.* Type I interferon response drives neuroinflammation and synapse loss in Alzheimer disease. *Journal of Clinical Investigation* **130**, 1912–1930 (2020).
86. Licht-Murava, A. *et al.* Astrocytic TDP-43 dysregulation impairs memory by modulating antiviral pathways and interferon-inducible chemokines. *Sci Adv* **9**, (2023).
87. Crow, Y. J. CNS disease associated with enhanced type I interferon signalling. *Lancet Neurol* **23**, 1158–1168 (2024).
88. Buckley, M. T. *et al.* Cell-type-specific aging clocks to quantify aging and rejuvenation in neurogenic regions of the brain. *Nat Aging* **3**, 121–137 (2022).
89. Hur, J.-Y. *et al.* The innate immunity protein IFITM3 modulates γ-secretase in Alzheimer's disease. *Nature* **586**, 735–740 (2020).
90. Roy, E. R. *et al.* Concerted type I interferon signaling in microglia and neural cells promotes memory impairment associated with amyloid β plaques. *Immunity* **55**, 879-894.e6 (2022).
91. Wang, Q. *et al.* Brain derived β-interferon is a potential player in Alzheimer's disease pathogenesis and cognitive impairment. *Alzheimers Res Ther* **16**, 271 (2024).
92. Wang, Q. *et al.* Brain derived β-interferon is a potential player in Alzheimer's disease pathogenesis and cognitive impairment. *Alzheimers Res Ther* **16**, 271 (2024).
93. Garthe, A. & Kempermann, G. An old test for new neurons: refining the Morris water maze to study the functional relevance of adult hippocampal neurogenesis. *Front Neurosci* **7**, (2013).
94. Kalamakis, G. *et al.* Quiescence Modulates Stem Cell Maintenance and Regenerative Capacity in the Aging Brain. *Cell* **176**, 1407-1419.e14 (2019).
95. Fernando, N. *et al.* Single-cell multiomic analysis reveals the involvement of Type I interferon-responsive CD8+ T cells in amyloid beta-associated memory loss. Preprint at https://doi.org/10.1101/2023.03.18.533293 (2023).

96. Chen, Y. & Colonna, M. Spontaneous and induced adaptive immune responses in Alzheimer's disease: new insights into old observations. *Curr Opin Immunol* **77**, 102233 (2022).
97. Chen, X. & Holtzman, D. M. Emerging roles of innate and adaptive immunity in Alzheimer's disease. *Immunity* **55**, 2236–2254 (2022).
98. Mason, H. D. & McGavern, D. B. How the immune system shapes neurodegenerative diseases. *Trends Neurosci* **45**, 733–748 (2022).
99. Meyer, M. *et al.* Cross reactivity of three T cell attracting murine chemokines stimulating the CXC chemokine receptor CXCR3 and their induction in cultured cells and during allograft rejection. *Eur J Immunol* **31**, 2521–7 (2001).
100. Loetscher, M., Loetscher, P., Brass, N., Meese, E. & Moser, B. Lymphocyte-specific chemokine receptor CXCR3: regulation, chemokine binding and gene localization. *Eur J Immunol* **28**, 3696–705 (1998).
101. Rustenhoven, J. & Kipnis, J. Smelling Danger: Olfactory Stem Cells Control Immune Defense during Chronic Inflammation. *Cell Stem Cell* **25**, 449–451 (2019).
102. Groh, J. *et al.* Microglia activation orchestrates CXCL10-mediated CD8+ T cell recruitment to promote aging-related white matter degeneration. *Nat Neurosci* **28**, 1160–1173 (2025).
103. Ma, W. *et al.* Type I interferon response in astrocytes promotes brain metastasis by enhancing monocytic myeloid cell recruitment. *Nat Commun* **14**, 2632 (2023).
104. Biber, K. *et al.* Functional expression of CXCR3 in cultured mouse and human astrocytes and microglia. *Neuroscience* **112**, 487–497 (2002).
105. Nelson, T. E. & Gruol, D. L. The chemokine CXCL10 modulates excitatory activity and intracellular calcium signaling in cultured hippocampal neurons. *J Neuroimmunol* **156**, 74–87 (2004).
106. Petrisko, T. J. *et al.* Neuronal CXCL10/CXCR3 Axis Mediates the Induction of Cerebral Hyperexcitability by Peripheral Viral Challenge. *Front Neurosci* **14**, (2020).
107. de Lucia, C. *et al.* Lifestyle mediates the role of nutrient-sensing pathways in cognitive aging: cellular and epidemiological evidence. *Commun Biol* **3**, 157 (2020).
108. Du Preez, A. *et al.* Impaired hippocampal neurogenesis in vitro is modulated by dietary-related endogenous factors and associated with depression in a longitudinal ageing cohort study. *Mol Psychiatry* **27**, 3425–3440 (2022).
109. Du Preez, A. *et al.* The serum metabolome mediates the concert of diet, exercise, and neurogenesis, determining the risk for cognitive decline and dementia. *Alzheimer's & Dementia* (2021) doi:10.1002/alz.12428.
110. Maruszak, A. *et al.* Predicting progression to Alzheimer's disease with human hippocampal progenitors exposed to serum. *Brain* **146**, 2045–2058 (2023).
111. Farmand, S., Ahmed, E., Zawar, H. A. & Thuret, S. Selenium deficiency negatively affects survival and integrity of human hippocampal progenitor cells. *Aging Brain* **7**, 100138 (2025).
112. Hafemeister, C. & Satija, R. Normalization and variance stabilization of single-cell RNA-seq data using regularized negative binomial regression. *Genome Biol* **20**, 296 (2019).

113. Wu, T. *et al.* clusterProfiler 4.0: A universal enrichment tool for interpreting omics data. *The Innovation* **2**, 100141 (2021).
114. Badia-I-Mompel, P. *et al.* decoupleR: ensemble of computational methods to infer biological activities from omics data. *Bioinformatics advances* **2**, vbac016 (2022).
115. Müller-Dott, S. *et al.* Expanding the coverage of regulons from high-confidence prior knowledge for accurate estimation of transcription factor activities. *Nucleic Acids Res* **51**, 10934–10949 (2023).
116. Türei, D. *et al.* Integrated intra- and intercellular signaling knowledge for multicellular omics analysis. *Mol Syst Biol* **17**, (2021).

Authors contribution

L.S.K and S.T. contributed equally and directed the research. T.A.D.N, L.S.K and S.T. designed the experiments. T.A.D.N wrote the manuscript, performed the majority of experiments, and conducted data analysis. T.A.D.N. and D.T.R. generated the single-cell RNA sequencing data in collaboration. A.B. collected and analysed RT-qPCR data. S.S. performed the morphological analysis of differentiated HPCs. H.L. helped design and generate the differentiation data as well as chemokine data. T.A.D.N and L.A.O'N. generated the ELISA and chemokine data. S.J. advised on STAT signalling and helped generate the STAT western blotting data. All authors read and revised the manuscript.

Acknowledgements

T.A.D.N was funded by the Wellcome Trust as part of the "Neuro-Immune Interactions in Health & Disease Wellcome Trust PhD Programme (218452/Z/19/Z)". The work was supported by a grant awarded to S.T. by the Medical Research Council UK (MR/S00484X/1). D.T.R. was supported by a PhD Studentship awarded by the Medical Research Council UK (MR/R015643/1), H.L. was supported by a grant from The Galen

and Hilary Weston Foundation awarded to S.T. We thank George Chennell and Chen Liang at the Wohl Cellular Imaging Centre at King's College London for providing excellent technical support and access to the high content imaging platform. In addition, we would like to thank the Genomics Research Platform at the R&D Department at the Guy's and St Thomas' NHS Foundation Trust. We thank Franziska Denk for her advice on the experimental design for the single-cell RNA sequencing. We thank Robert Köchl and Aritz Lasarte Cía for their advice on the experimental design of the chemotaxis experiments. We thank Josephine Eum for her advice on obtaining and processing the blood samples for the isolation of PBMCs. Finally, we thank Daniel Davies for his guidance on the cell staining protocol for the flow cytometry.

Ethics declaration

The authors declare that ethical standards prevailing at their institutions have been observed throughout this study.

Competing interests

The authors declare no competing interests.

Extended data

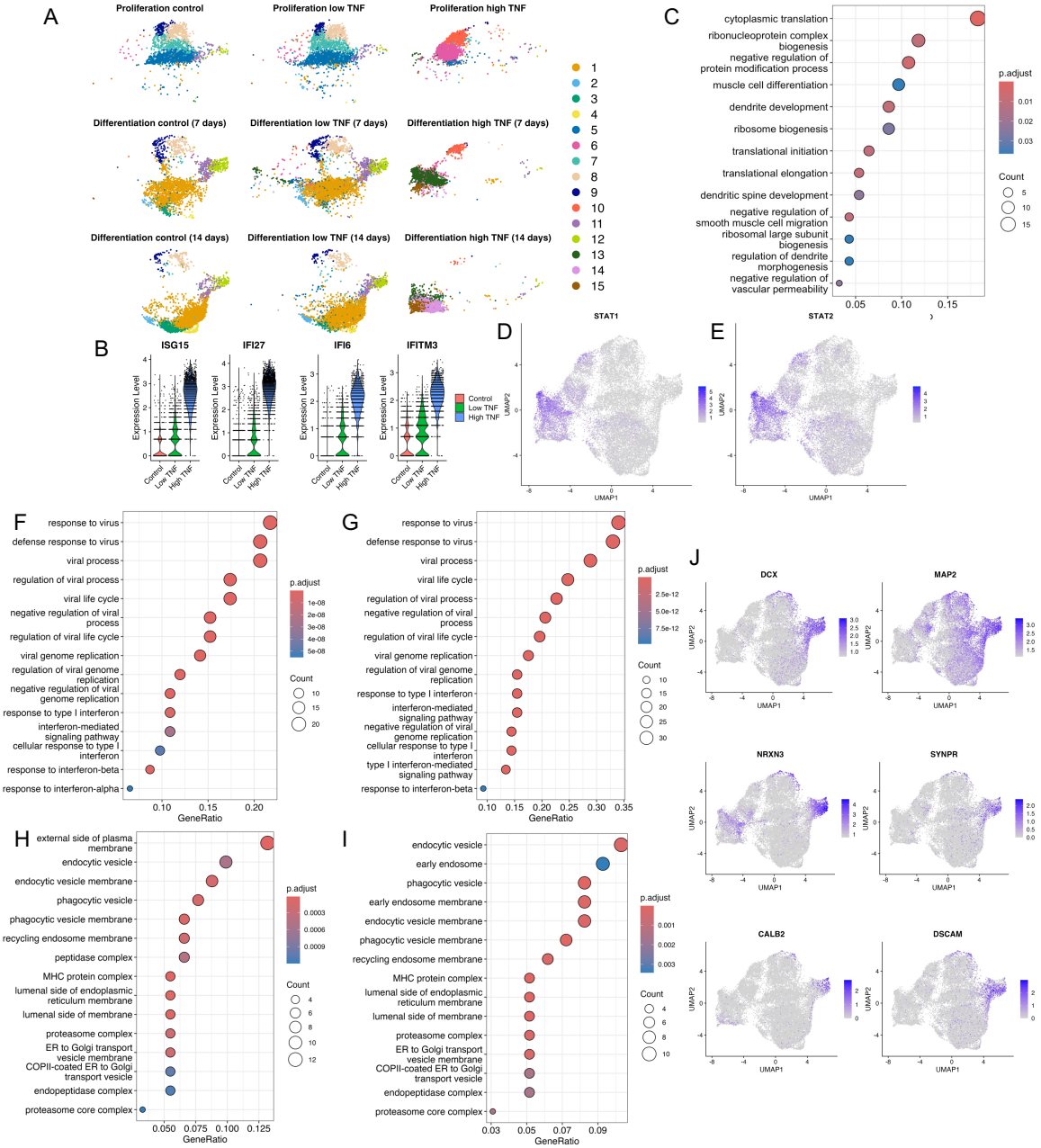

Extended data Fig. 1 | TNF-α drives the upregulation of type I IFN genes in HPCs. A UMAP plot showing transcriptional clustering of single cells split by samples. Colors indicate the 15 cell clusters identified. **B** Violin plots showing dose-dependent expression of the type I IFN stimulated genes ISG15, IFI27, IFI6, and IFITM3 in the HPCs treated for 48 hrs with vehicle (red), 0.1 ng/ml (low, green), or 1 ng/ml (high, blue) TNF-α. **C** Dot plot showing gene ontology (GO) enrichment analysis of biological processes terms based on the top 100 genes upregulated genes in cluster 5 as compared to cluster 6. **D** UMAP plot showing the predicted transcription factor activity of STAT1. **E** UMAP plot showing the predicted transcription factor activity of STAT2. **F** Dot plot showing gene ontology (GO) enrichment analysis of biological processes terms based on the top 100 genes upregulated genes in cluster 6 as compared to cluster 5. **G** Dot plot showing gene ontology (GO) enrichment analysis of biological processes terms based on the top 100 genes upregulated genes in cluster 10 as compared to cluster 7, 8, and 9. **H** Dot plot showing gene ontology (GO) enrichment analysis of cellular component terms based on the top 100 genes upregulated genes in cluster 6 as compared to cluster 5. **I** Dot plot showing gene ontology (GO) enrichment analysis of cellular component terms based on the top 100 genes upregulated genes in cluster 10 as compared to cluster 7, 8, and 9. **J** UMAP plots showing the expression of neuronal genes *DCX*, *MAP2*, *NRXN3*, *CALB2*, and *DSCAM*.

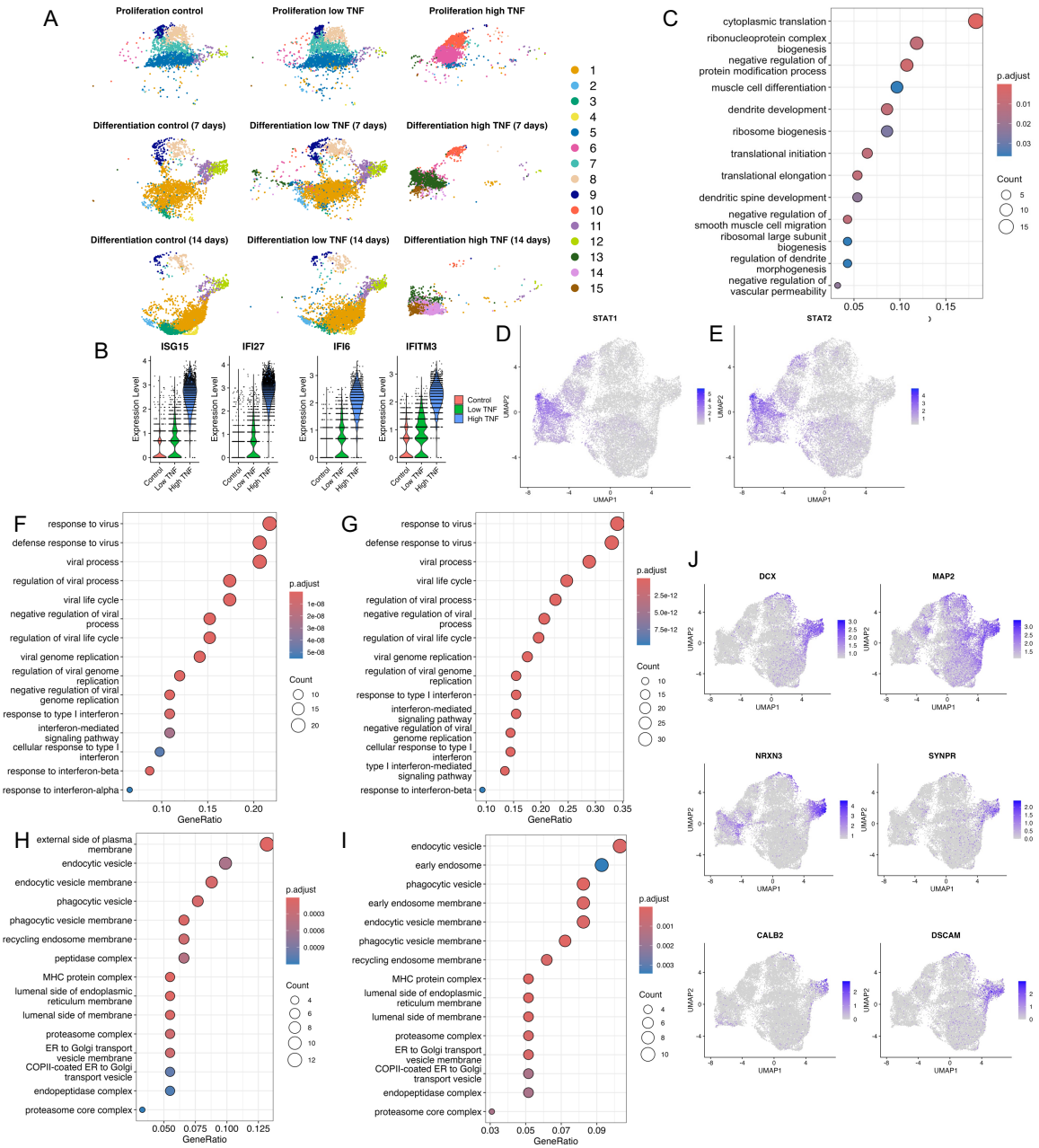

Extended data Fig. 2 | TNF-α drives the upregulation of type I IFN genes in HPCs. A UMAP plot showing transcriptional clustering of single cells split by samples. Colors indicate the 15 cell clusters identified. **B** Violin plots showing dose-dependent expression of the type I IFN stimulated genes ISG15, IFI27, IFI6, and IFITM3 in the HPCs treated for 48 hrs with vehicle (red), 0.1 ng/ml (low, green), or 1 ng/ml (high, blue) TNF-α. **C** Dot plot showing gene ontology (GO) enrichment analysis of biological processes terms based on the top 100 genes upregulated genes in cluster 5 as compared to cluster 6. **D** UMAP plot showing the predicted transcription factor activity of STAT1. **E** UMAP plot showing the predicted transcription factor activity of STAT2. **F** Dot plot showing gene ontology (GO) enrichment analysis of biological processes terms based on the top 100 genes upregulated genes in cluster 6 as compared to cluster 5. **G** Dot plot showing gene ontology (GO) enrichment analysis of biological processes terms based on the top 100 genes upregulated genes in cluster 10 as compared to cluster 7, 8, and 9. **H** Dot plot showing gene ontology (GO) enrichment analysis of cellular component terms based on the top 100 genes upregulated genes in cluster 6 as compared to cluster 5. **I** Dot plot showing gene ontology (GO) enrichment analysis of cellular component terms based on the top 100 genes upregulated genes in cluster 10 as compared to cluster 7, 8, and 9. **J** UMAP plots showing the expression of neuronal genes *DCX*, *MAP2*, *NRXN3*, *CALB2*, and *DSCAM*.

Supplementary information

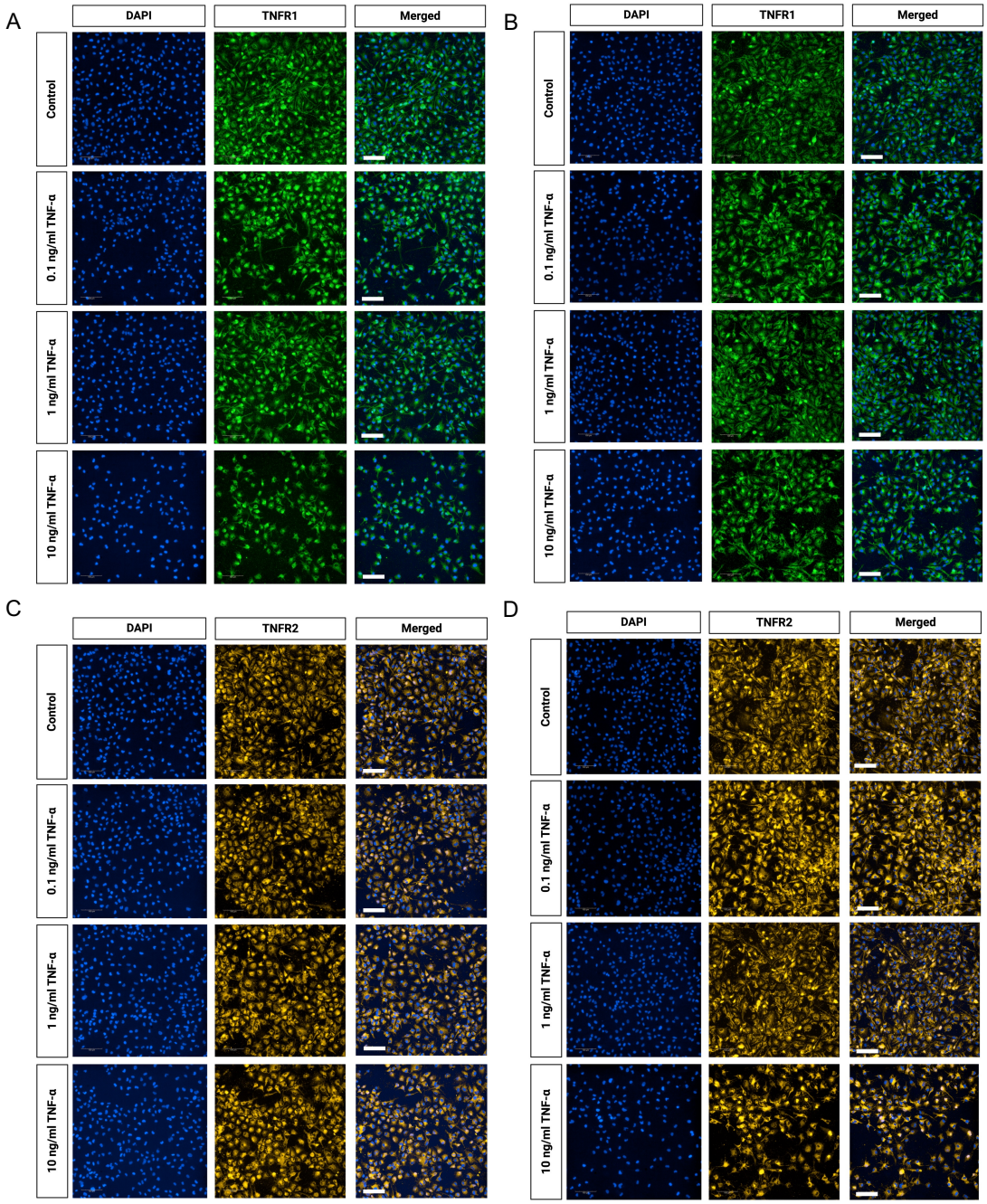

Supplementary data Fig. 1 | TNFR expression on human HPCs treated ± TNF-α. A and **B** Representative images of three independent experiments with similar results showing the expression of TNFR1 (green) on HPCs treated ± TNF-α for **A** 24 hrs or **B** 48 hrs. **C** and **D** Representative images of three independent experiments with similar results showing the expression of TNFR2 (orange) on HPCs treated ± TNF-α for **C** 24 hrs or **D** 48 hrs. Scalebar = 100 µm. DAPI; 4′,6- diamidino-2-phenylindole, HPC; hippocampal progenitor cells, TNFR1; tumour necrosis factor receptor 1. Images are representative of three independent experiments.

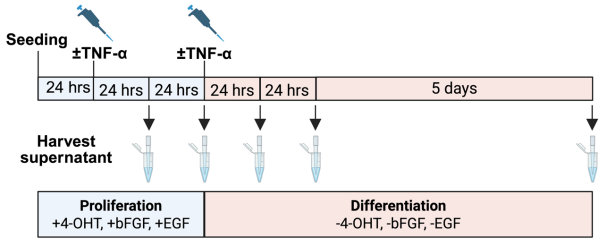

Supplementary data Fig. 2 | Schematic overview of the experimental design for harvesting supernatant from HPCs and their differentiated progeny. The day following the seeding, the proliferating HPCs were treated ± TNF-α (0.1 ng/ml, 1 ng/ml, or 10 ng/ml). After 24 hours the supernatant was harvested. After 48 hours of treatment, the supernatant was harvested, and the media changed to induce differentiation (removal of 4-OHT, bFGF, and EGF) ± TNF-α (0.1 ng/ml, 1 ng/ml, or 10 ng/ml). The supernatant of the differentiating cells was harvested after 24 hours, 48 hours, or 7 days of differentiation. 4-OHT; 4- hydroxytamoxifen, bFGF; basic fibroblast growth factor, EGE; epidermal growth factor.

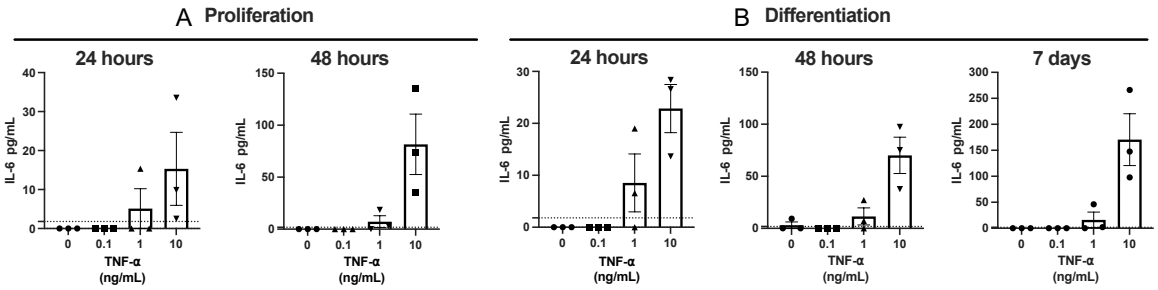

Supplementary data Fig. 3 | ELISA measurement of IL-6 in the supernatant of HPCs and their differentiated progeny treated with TNF-α. A Concentrations of IL-6 in the supernatant of proliferating HPCs 24 hours and 48 hours after TNF-α treatment respectively. **B** IL-6 in the supernatant of differentiating HPCs 24 hours, 48 hours, and 7 days after TNF-α treatment respectively. Data is represented as mean ± SEM of three independent experiments.

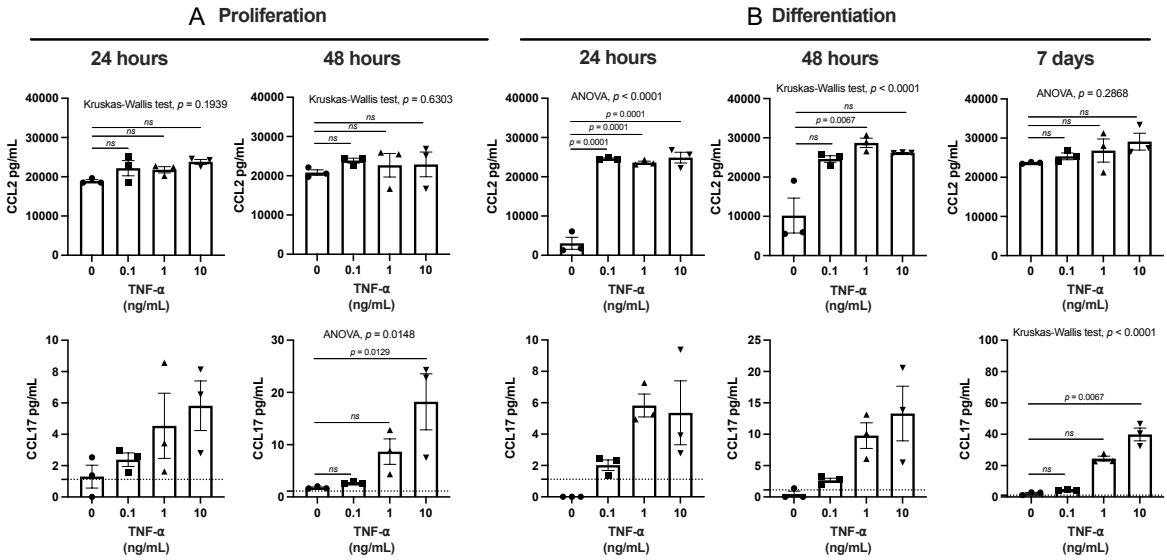

Supplementary data Fig. 4 | CCL2 and CCL17 levels in the supernatant of HPCs and their differentiated progeny treated with TNF-α. A Concentrations of CCL2 (upper panel) and CCL17 (lower panel) in the supernatant of proliferating HPCs 24 hours and 48 hours after TNF-α treatment respectively. **B** CCL2 (upper panel) and CCL17 (lower panel) in the supernatant of differentiating HPCs 24 hours, 48 hours, and 7 days after TNF-α treatment respectively. Data is represented as mean ± SEM of three independent experiments. Statistical test: Kruskal-Wallis test followed by Dunn's post hoc correction or one-way ANOVA followed by Bonferroni's multiple comparisons as indicated above the graphs. Stripped lines mark the detection limit for CCL17 (1.12 pg/ml).

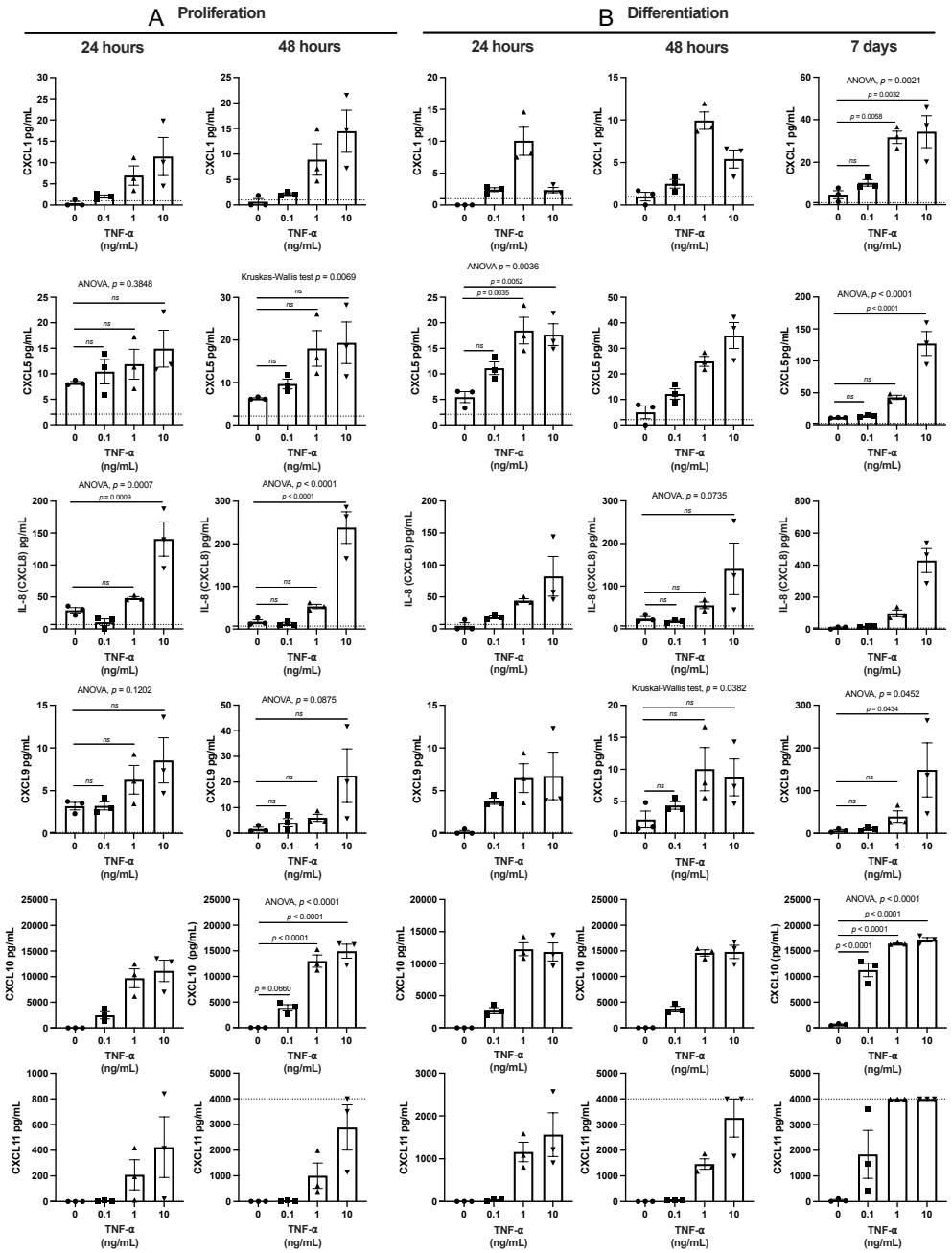

Supplementary data Fig. 5 | CXC chemokine levels in the supernatant of HPCs and their differentiated progeny treated with TNF-α. A Concentrations of CXCL1, CXCL5, IL-8, CXCL9, CXCL10, and CXCL11 in the supernatant of proliferating HPCs 24 hours and 48 hours after TNF-α treatment. **B** CXCL1, CXCL5, IL-8, CXCL9, CXCL10, and CXCL11 levels in the supernatant of differentiating HPCs 24 hours, 48 hours, and 7 days after TNF-α treatment respectively. Data is represented as mean ± SEM of three independent experiments. Statistical test: Kruskal-Wallis test followed by Dunn's post hoc correction or one-way ANOVA followed by Bonferroni's multiple comparisons as indicated above the graphs. Stripped lines mark the detection limits (lower limit for CXCL1: <0.99 pg/ml, lower limit for CXCL5: <2.07 pg/ml, lower limit for CXCL8: <6.86 pg/ml, lower limit for CXCL9: <0.098 pg/ml, lower limit for CXCL10: <23.44 pg/ml, lower limit for CXCL11 <2.13 pg/ml, and upper limit for CXCL11 > 4000 pg/ml). For visualisation data points below the detection limit were set to zero, and data points above the upper detection limit for CXCL11 were set to the limit of 4000 pg/ml

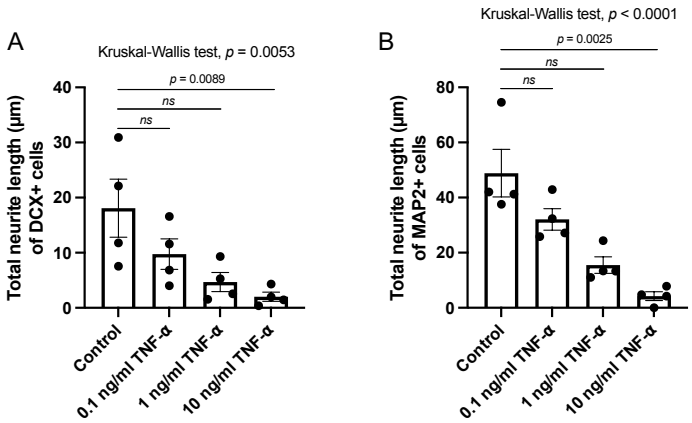

Supplementary data Fig. 6 | Chronic TNF-α dose-dependently decreases the neurite length of DCX+ and MAP2+ differentiating HPCs. Quantification of the total neurite length (µm) of **A** DCX+ cells and **B** MAP2+ cells after seven days of differentiation ± chronic treatment with 0.1, 1, or 10 ng/ml TNF-α. Data represent mean ± SEM from four independent experiments. Statistical analysis: Kruskal-Wallis test followed by Dunn's post hoc correction.

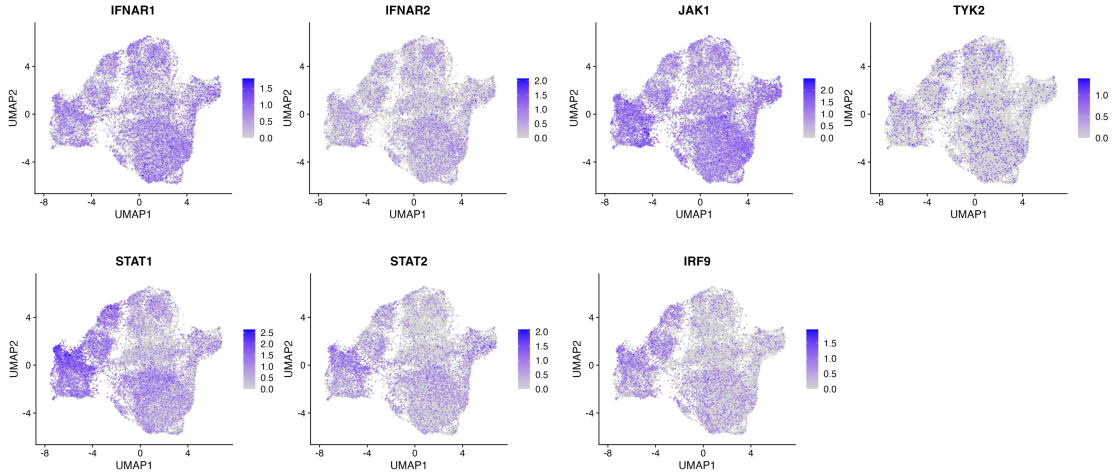

Supplementary data Fig. 7 | Molecular machinery to respond to type I interferons. UMAP plots showing the expression of genes constituting the molecular machinery needed to respond to type I interferons: *IFNAR1*, *IFNAR2*, *JAK1*, *TYK2*, *STAT1*, *STAT2*, and *IRF9*.

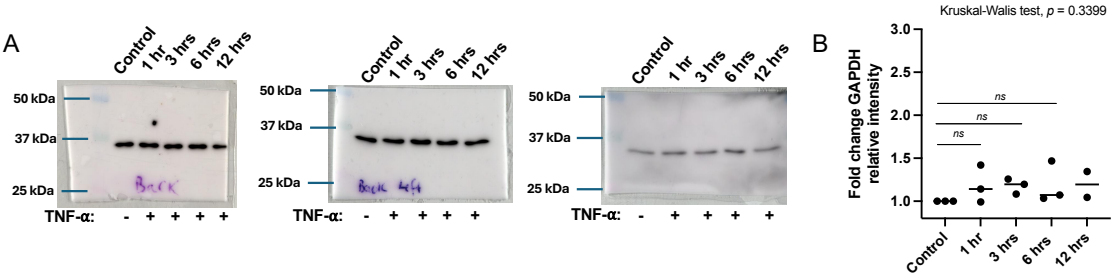

Supplementary data Fig. 8 | TNF-α does not regulate the expression of the housekeeping gene GAPDH. A The original, uncropped Western blot images for the three experimental replicates probing for GAPDH. The HPCs were treated with 1 ng/ml TNF-α for 1 hr, 3 hrs, 6 hrs, and 12 hrs. The molecular weight markers are included for reference (Precision Plus Protein Kaleidoscope Prestained Protein Standards). **B** Quantification of the GAPDH band intensities in **A**. Data represent mean ± SEM from three independent experiments. Statistical analysis: Kruskal-Wallis test followed by Dunn's post hoc correction.

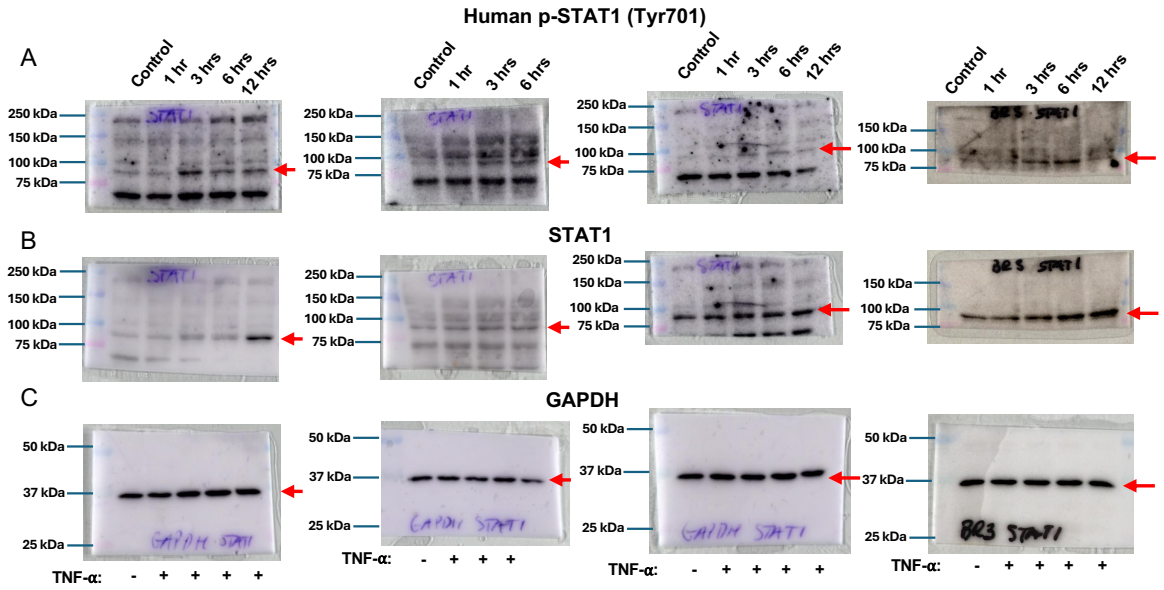

Supplementary data Fig. 9 | Uncropped Western blots corresponding to Figure 4A and 4B. A The original, uncropped Western blot images for the four experimental replicates probing for pSTAT1 (Tyr701). **B** The original, uncropped Western blot images for the experimental replicates probing for total STAT1. **C** The original, uncropped Western blot images for the experimental replicates probing for the loading control GAPDH. The HPCs were treated with 1 ng/ml TNF-α for 1 hr, 3 hrs, 6 hrs, and 12 hrs. The molecular weight markers are included for reference (Precision Plus Protein Kaleidoscope Prestained Protein Standards). The red arrows indicate the band of interest on the images.

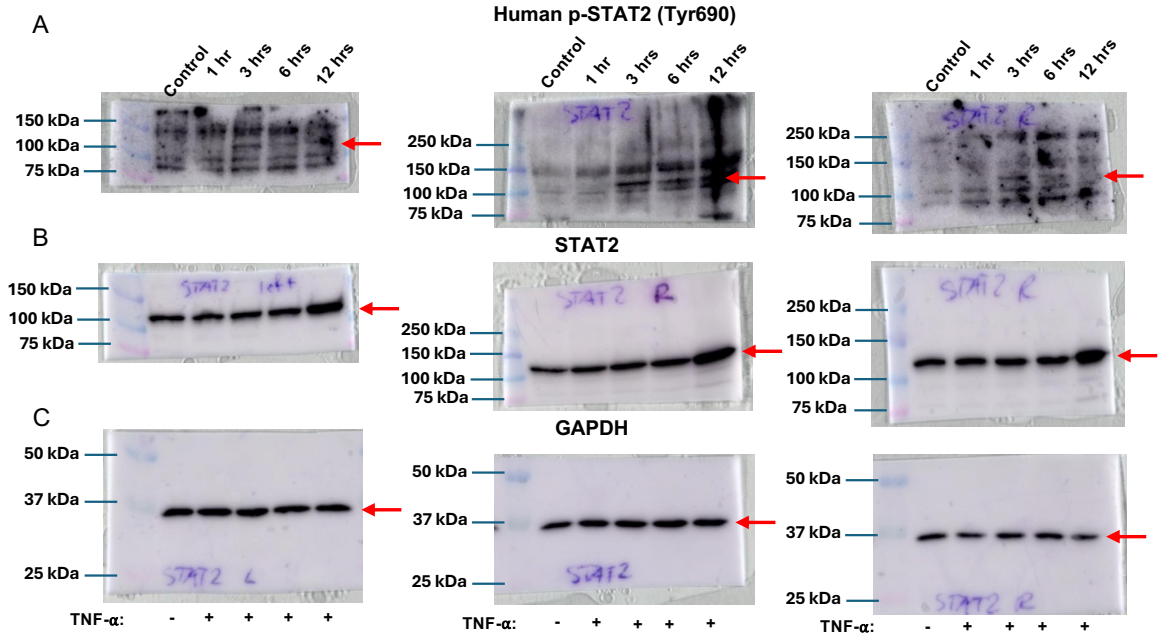

Supplementary data Fig. 10 | Uncropped Western blots corresponding to extended data Figure 1A and 1B. A The original, uncropped Western blot images for the four experimental replicates probing for pSTAT2 (Tyr690). **B** The original, uncropped Western blot images for the experimental replicates probing for total STAT2. **C** The original, uncropped Western blot images for the experimental replicates probing for the loading control GAPDH. The HPCs were treated with 1 ng/ml TNF-α for 1 hr, 3 hrs, 6 hrs, and 12 hrs. The molecular weight markers are included for reference (Precision Plus Protein Kaleidoscope Prestained Protein Standards). The red arrows indicate the band of interest on the images.

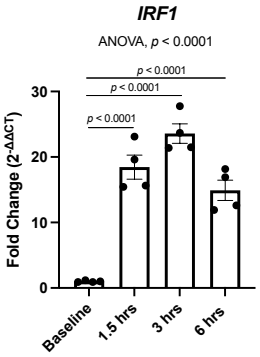

Supplementary data Fig. 11 | HPCs upregulate the expression of transcription factor *IRF1* in response to TNF-α. RT-qPCR data showing the relative gene expression of *IRF1* in HPCs treated ± 1 ng/ml TNF-α for 1.5 hrs, 3 hrs, or 6 hrs. Data is represented as mean ± SEM of four independent experiments. Statistical analysis: one-way ANOVA followed by Bonferroni's multiple comparisons.

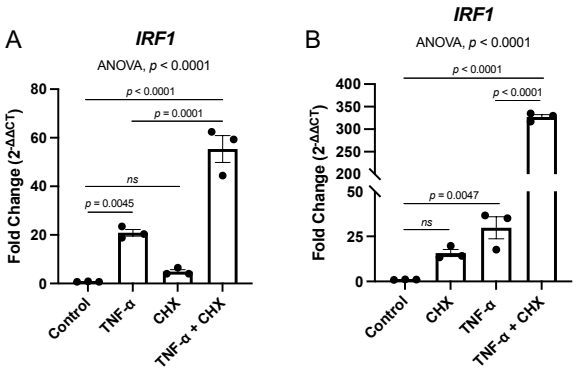

Supplementary data Fig. 12 | *De novo* protein synthesis is dispensable for TNF-α-induced upregulation of *IRF1*. A RT-qPCR data showing the relative gene expression of *IRF1* in HPCs treated for 3 hrs with 10 µg/ml CHX or DMSO followed by treatment ± 1 ng/ml TNF-α. Data is represented as mean ± SEM of three independent experiments. Statistical analysis: one-way ANOVA followed by Bonferroni's multiple comparisons. **B** RT-qPCR data showing the relative gene expression of *IRF1* in HPCs treated for 6 hrs with 10 µg/ml CHX or DMSO ± 1 ng/ml TNF-α. Data is represented as mean ± SEM of three independent experiments. Statistical analysis: one-way ANOVA followed by Bonferroni's multiple comparisons

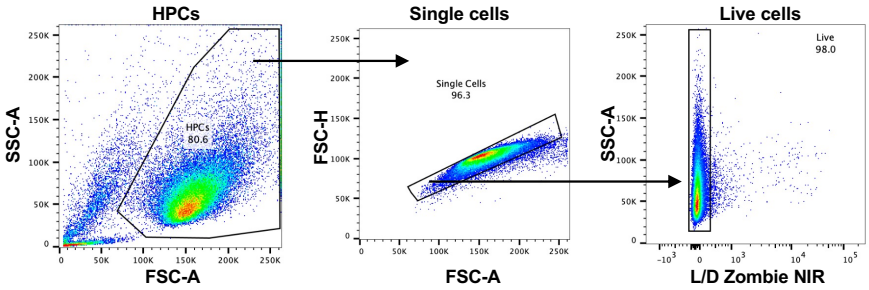

Supplementary data Fig. 13 | Gating strategy for investigating the cell surface expression of proteins on HPCs. Representative gating strategy to investigate the expression of cell surface proteins on live, single HPCs. Cells were first gated based on forward scatter (FSC) and side scatter (SSC) to exclude debris and identify the main cell population. Singlets were then selected using FSC-A vs. FSC-H to eliminate doublets. Live cells were identified by negative selection using the live/dead viability dye Zombie NIR.

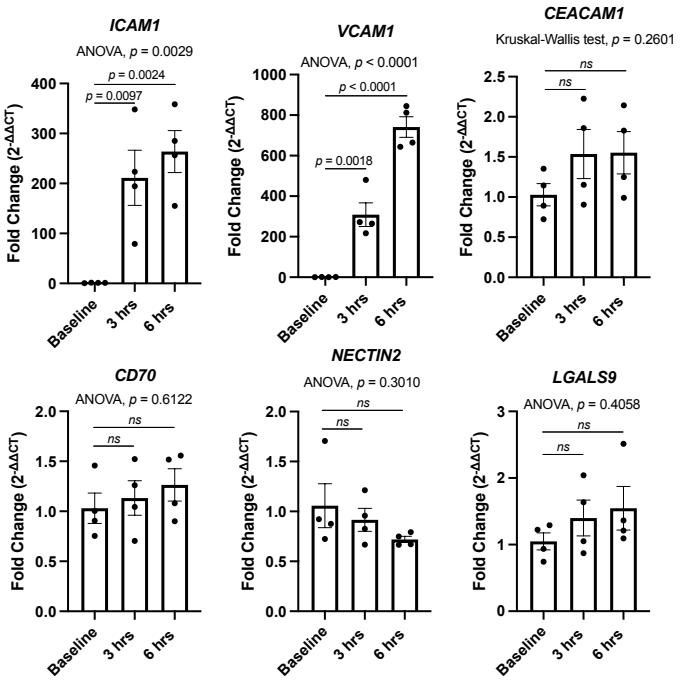

Supplementary data Fig. 14 | HPCs upregulate molecules implicated in T cell crosstalk in response to TNF-α. RT-qPCR data showing the relative gene expression of *ICAM1, VCAM1, CEACAM1, CD70, NECTIN2, and LGALS9* in HPCs treated ± 1 ng/ml TNF-α for 1.5 hrs, 3 hrs, or 6 hrs. Data is represented as mean ± SEM of four independent experiments. Statistical analysis: one-way ANOVA followed by Bonferroni's multiple comparisons or Kruskal-Wallis test followed by Dunn's post hoc correction as indicated above the graphs.

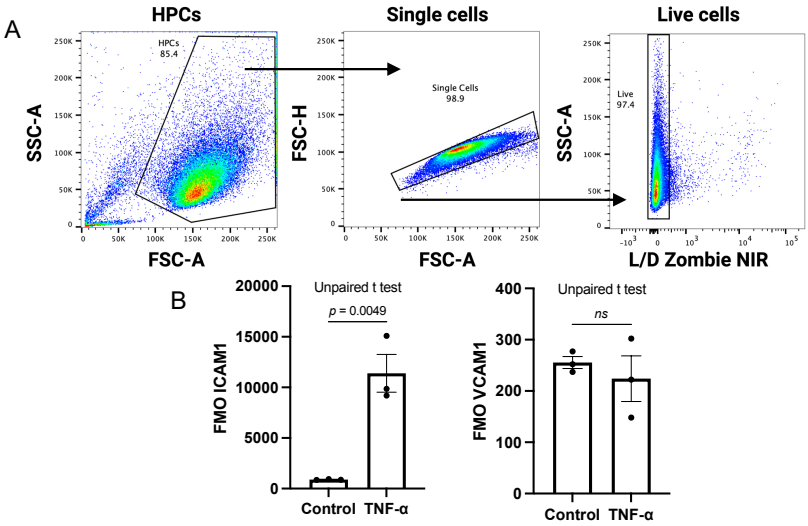

Supplementary data Fig. 15 | Evaluating HPC cell surface ICAM1 and VCAM1 levels in response to TNF-α. A Gating strategy for investigating the cell surface expression of proteins on HPCs. Representative gating strategy to investigate the expression of cell surface proteins on live, single HPCs. Cells were first gated based on forward scatter (FSC) and side scatter (SSC) to exclude debris and identify the main cell population. Singlets were then selected using FSC-A vs. FSC-H to eliminate doublets. Live cells were identified by negative selection using the live/dead viability dye Zombie NIR. **B** Cell surface expression of ICAM1 and VCAM1 quantified by measuring the mean fluorescence intensity (MFI) on HPCs treated 24 hrs ± 1 ng/ml TNF-α using flow cytometry. Data represent mean ± SEM. Statistical analysis: two-tailed, unpaired t test.

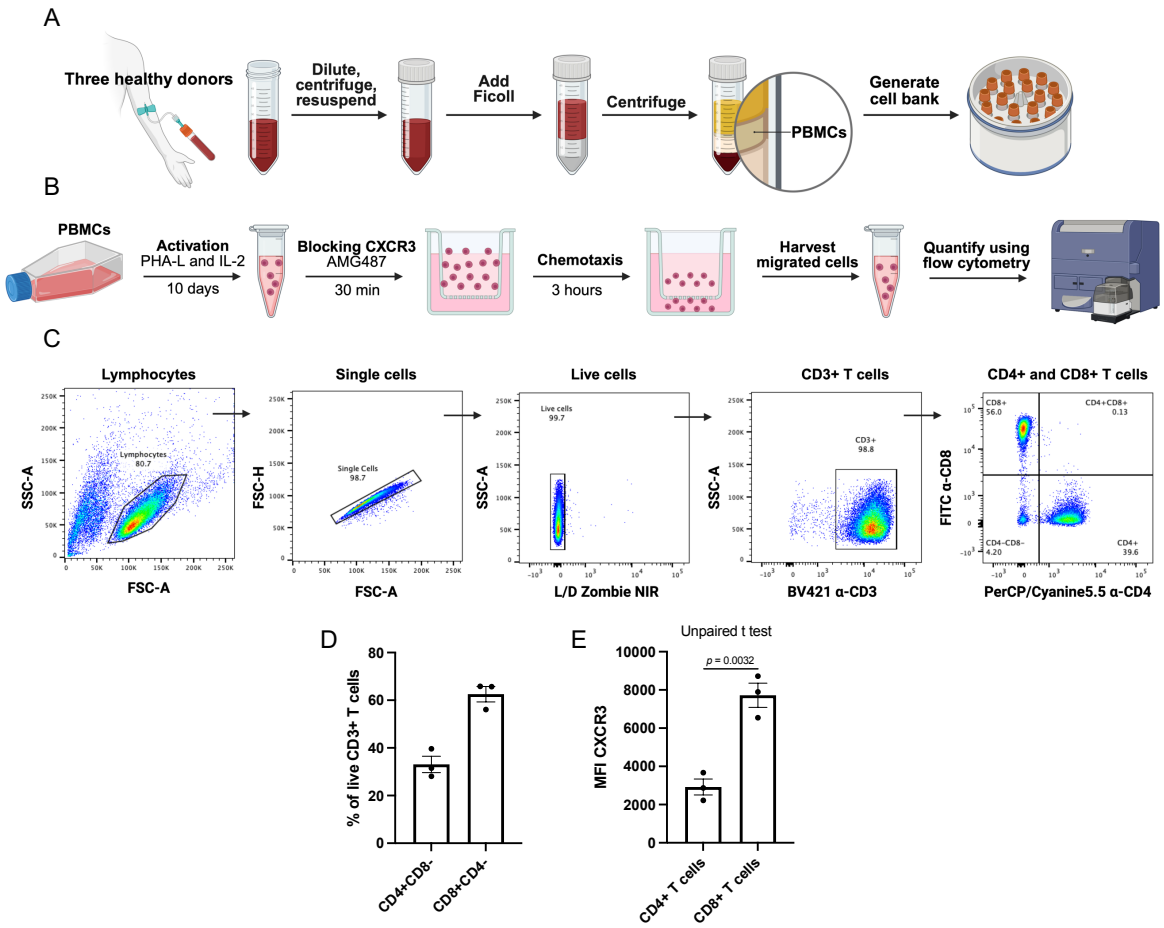

Supplementary data Fig. 16 | Transwell chemotaxis assay using primary, human T cells to study CXCR3-dependent chemotaxis. A PBMS were isolated from leukocytes cones from three healthy donors using a Ficoll-Paque desity gradient and a cell bank was generated for each donor. **B** Schematic overview of the T cell chemotaxis assay. PBMCs were thawed and the following day activated using IL-2 and PHA-L for 48 hours. Cells were kept in culture for ten days and media was replaced every 48 hours with IL-2. On the day of the experiment, the cells were harvested and washed before incubation for 30 minutes with 1 μM CXCR3 antagonist AMG487 or DMSO. The lower chamber contained the chemoattractant and the upper wells the activated cells. After three hours the cells migrated to the lower chamber were harvested and stained with antibodies for flow cytometry analysis. The phenotype and number of migrated cells were quantified using a high throughput sampler connected to a flow cytometer. **C** Representative gating strategy to identify CD4+ and CD8+ T cells. **D** Percentage of cell subsets after cell activation protocol. Data is represented as mean ± SEM of three healthy donors. **E** Quantification of CXCR3 MFI (median) between CD4+ T cells and CD8+ T cells. Data is represented as mean ± SEM of three healthy donors. Statistical analysis: unpaired, two-tailed, parametric t-test

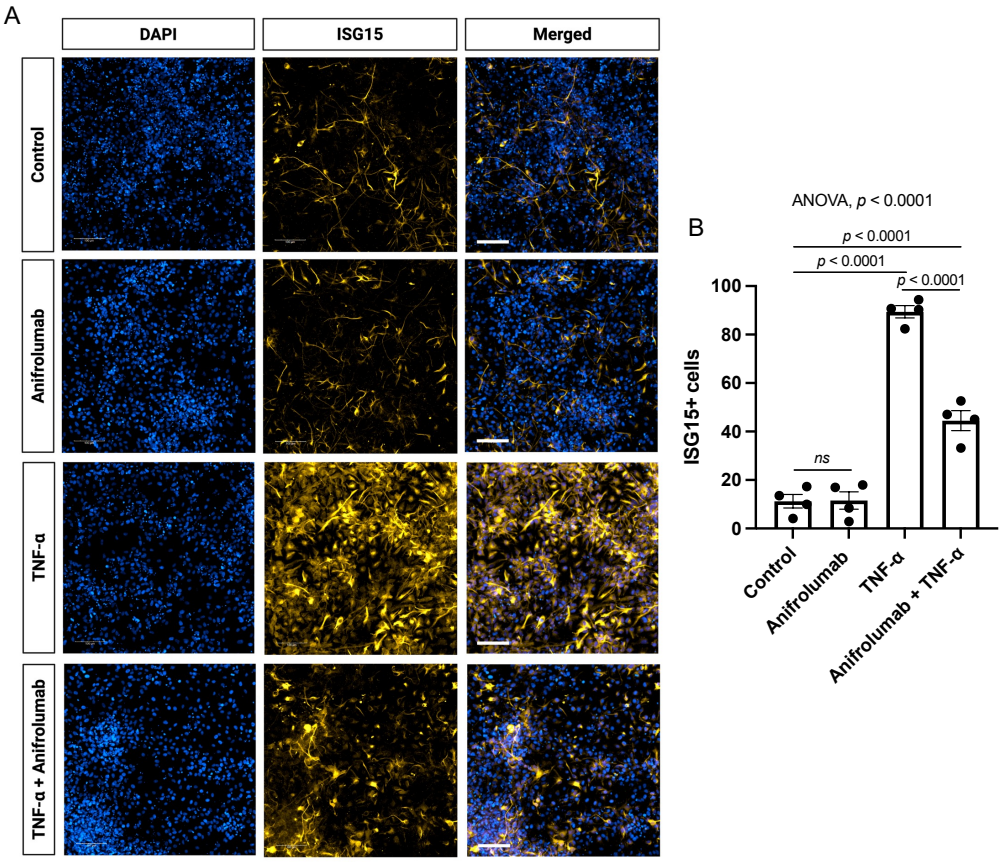

Supplementary data Fig. 17 | Blocking IFNAR decrease the upregulation of ISG15+ differentiating HPCs in response to chronic TNF-α. **A** Representative images showing the expression of ISG15 (orange) on seven days differentiated HPCs treated chronically ± 1 TNF-α ± 10 µg/ml anifrolumab. Scale bar represents 100 µm. **B** Quantification of the percentage of ISG15+ cells based on **A**. Data represent mean ± SEM from four independent experiments. Statistical analysis: one-way ANOVA followed by Bonferroni's multiple comparisons.